Microscopy and Microanalysis (2018), **24**, 406–419
doi:10.1017/S1431927618012382

Microscopy AND Microanalysis

Review Article

Biological Applications at the Cutting Edge of Cryo-Electron Microscopy

Rebecca S. Dillard[1], Cheri M. Hampton[1†], Joshua D. Strauss[1], Zunlong Ke[1,2], Deanna Altomara[1], Ricardo C. Guerrero-Ferreira[1‡], Gabriella Kiss[1††] and Elizabeth R. Wright[1,3,‡‡]

[1]Division of Pediatric Infectious Diseases, Emory University School of Medicine, Children's Healthcare of Atlanta, Atlanta, GA 30322, USA, [2]School of Biological Sciences, Georgia Institute of Technology, Atlanta, GA 30332, USA and [3]Robert P. Apkarian Integrated Electron Microscopy Core, Emory University, Atlanta, GA 30322, USA

Abstract

Cryo-electron microscopy (cryo-EM) is a powerful tool for macromolecular to near-atomic resolution structure determination in the biological sciences. The specimen is maintained in a near-native environment within a thin film of vitreous ice and imaged in a transmission electron microscope. The images can then be processed by a number of computational methods to produce three-dimensional information. Recent advances in sample preparation, imaging, and data processing have led to tremendous growth in the field of cryo-EM by providing higher resolution structures and the ability to investigate macromolecules within the context of the cell. Here, we review developments in sample preparation methods and substrates, detectors, phase plates, and cryo-correlative light and electron microscopy that have contributed to this expansion. We also have included specific biological applications.

Key words: cryo-electron microscopy (cryo-EM), cryo-electron tomography (cryo-ET), cryo-correlative light and electron microscopy (cryo-CLEM), transmission electron microscopy (TEM), vitrification, phase plates, direct electron detectors

(Received 6 March 2018; revised 10 May 2018; accepted 14 June 2018)

Introduction

Cryo-electron microscopy (cryo-EM) technologies were pioneered in order to retain specimen hydration and reduce electron-beam damage to the specimen during direct imaging and electron diffraction in the transmission electron microscope (TEM) (Taylor & Glaeser, 1974). Initial work focused on catalase crystals preserved in a thin film of vitreous ice (Taylor & Glaeser, 1974). Subsequently, suspensions of viruses and other samples were vitrified and imaged, functionally extending cryo-EM to structural investigations of broad ranges of targets (Dubochet et al., 1983; Lepault et al., 1983; McDowall et al., 1983; Adrian et al., 1984). Most aqueous samples are prepared for cryo-EM or cryo-electron tomography (cryo-ET) by first applying a small aliquot of a suspension to an electron microscopy (EM) grid, blotting the grid to near dryness, and then rapidly plunge-freezing it in liquid ethane or liquid propane cooled to cryogenic temperatures. This method effectively preserves the biological sample in a thin layer of vitreous, non-crystalline ice in a near native state (Lepault et al., 1983; Dubochet et al., 1988). Continued developments to specimen preservation equipment and methods by research groups and EM manufacturers have improved the quality and reproducibility of the cryo-EM grids prepared.

The cryo-preserved specimens are then loaded into grid-holders, e.g. cryo-holders, which maintain the specimen at close to liquid nitrogen temperatures in order to minimize the devitrification or warming of the specimen. There have been many improvements made to these holders since their introduction in the late 1970s. Many of the cryo-holders available may be used in standard side-entry microscopes. In order to preserve specimen integrity and to facilitate high-throughput data collection, EM companies began to design and produce instruments with "multi-specimen" cartridge-style systems in which 3–12 individual specimens can be loaded into the column of the microscope. Simultaneously, improvements to overall microscope stability, the use of field emission electron sources, computer control, and the automation of standard functions enabled the beginning of the "resolution revolution in cryo-EM" (Kuhlbrandt, 2014), by facilitating the acquisition of high quality EM data both on film and charge coupled device (CCD) cameras via automated routines (Hewat & Neumann, 2002; Stagg et al., 2006).

Samples prepared for single particle analysis (SPA) cryo-EM are typically purified homogeneous proteins, macromolecules, or viruses. Ideally, the sample is vitrified with particles in random orientations within a uniform layer of ice. After imaging, the

Author for correspondence: Elizabeth R. Wright, E-mail: erwrigh@emory.edu
† Current address: Materials and Manufacturing Directorate, Air Force Research Laboratory, Wright-Patterson AFB, Ohio 45433, USA.
‡ Current address: Center for Cellular Imaging and NanoAnalytics (C-CINA), Biozentrum, University of Basel, Mattenstrasse 26, 4058 Basel, Switzerland.
†† Current address: Thermo Fisher Scientific, 5350 NE Dawson Creek Drive, Hillsboro, OR 97124, USA.
‡‡ Current address: Department of Biochemistry, University of Wisconsin, Madison, WI 53706, USA.

Cite this article: Dillard RS, Hampton CM, Strauss JD, Ke Z, Altomara D, Guerrero-Ferreira RC, Kiss G, Wright ER (2018) Biological Applications at the Cutting Edge of Cryo-Electron Microscopy. *Microsc Microanal* **24**(4): 406–419. doi: 10.1017/S1431927618012382

particles are identified, aligned and classified, and reconstructed to produce a three-dimensional (3D) map (Cheng et al., 2015). Heterogeneous samples, such as pleomorphic viruses, bacteria, or mammalian cells are more readily studied using cryo-ET, in which a collection of images of a vitrified single feature on the grid is acquired at various tilts, producing a tilt series. The images of the tilt series are then computationally back-projected to generate a 3D reconstruction, or tomogram, of the sample (Oikonomou & Jensen, 2017). Homogenous components within the tomogram may be extracted and further analyzed using sub-tomogram averaging (Wan & Briggs, 2016).

Recent advances in sample preparation, imaging, and data processing have led to a dramatic expansion of cryo-EM in structural biology (Cheng et al., 2015; Nogales, 2015). The workflow for structure determination by cryo-EM is outlined in Figure 1. Sample optimization is achieved by one of several freezing steps. Vitrification of a thin film sample for SPA cryo-EM or cryo-ET is accomplished by plunge freezing. Larger sample volumes, including confluent cell layers and tissue, may be vitrified using pressure by high pressure freezing (Dahl & Staehelin, 1989; Dubochet, 1995; Studer et al., 2008) or self-pressurized rapid freezing (Leunissen & Yi, 2009; Han et al., 2012*b*; Grabenbauer et al., 2014). The sample may be further processed after vitrification by thinning [cryo-focused ion beam milling (cryo-FIB) or cryo-sectioning] or examined by cryo-correlative light and electron microscopy (cryo-CLEM) before cryo-ET imaging and image processing. In this review, we discuss some of the recent advances at various steps of this workflow, which we have used to improve imaging of biological specimens. These include the use of new substrates and methods for sample preparation, phase plates and direct electron detectors for cryo-EM image acquisition, and the application of cryo-CLEM, which combines spatiotemporal information about the sample from fluorescence light microscopy with structural information from cryo-EM. There have, of course, been many other developments in techniques and data processing that are described elsewhere (Bai et al., 2015; Binshtein & Ohi, 2015; Fernandez-Leiro & Scheres, 2016; Frank, 2017; Murata & Wolf, 2018).

Substrates and Specimen Preparation

One of the essential components of high-quality, high-resolution cryo-EM is reproducible and robust sample preparation. Cryo-EM samples are typically applied to an EM grid consisting of an amorphous holey carbon film supported by a metal mesh. The grid is then blotted to remove excess liquid and plunge-frozen in a liquid cryogen ("plunge freezing" in Fig. 1), suspending the sample in a layer of vitreous ice. This process preserves the close-to-native-state structure of the hydrated specimen, but can have low throughput and be unpredictable in terms of ice thickness and particle distribution. Additionally, it has been shown that irradiation in the EM leads to deformation of the amorphous carbon, causing sample movement and hence blurred images (Glaeser et al., 2011; Brilot et al., 2012; Russo & Passmore, 2016*b*).

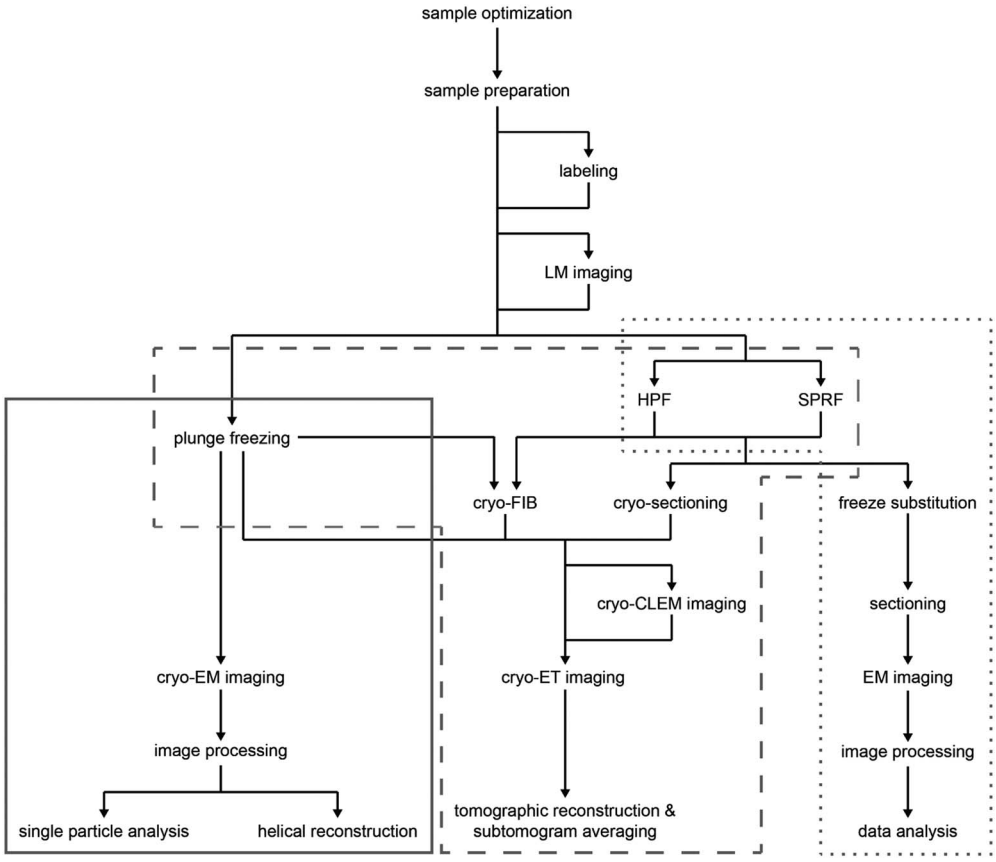

Figure 1. Cryo-electron microscopy (cryo-EM) workflow. Schematic illustration of options for cryo-EM sample preparation, imaging, and data processing. Solid gray box indicates methods typically used for single particle analysis; dashed gray box indicates methods typically used for cryo-electron tomography (cryo-ET); dotted gray box indicates methods typically used for conventional EM sectioning. LM, light microscopy; HPF, high pressure freezing; SPRF, self-pressurized rapid freezing; FIB, focused ion beam; CLEM, correlated light and electron microscopy.

https://doi.org/10.1017/S1431927618012382 Published online by Cambridge University Press

Recently, several new sample purification methods, substrates, and grid preparation systems have been developed to optimize performance during imaging, including affinity capture systems, gold grids, and advanced vitrification devices.

Cryo-EM single particle reconstructions are based on averaging projections of thousands of identical particles in random orientations (Guo & Jiang, 2014; Cheng et al., 2015; Doerr, 2015; Frank, 2017). Homogeneity of the sample is therefore extremely important although such purification can be challenging. Cross-linking has been used to stabilize many heterogeneous samples for cryo-EM, such as the proteasome (Lasker et al., 2012), spliceosome (Agafonov et al., 2016; Wan et al., 2016; Bertram et al., 2017), and membrane complexes (Fiedorczuk et al., 2016; Kosinski et al., 2016). These studies combined cryo-EM with cross-linking mass spectrometry, which provides even further detail about residues that are in close proximity (Schmidt & Urlaub, 2017). An additional method for reducing heterogeneity, called GraFix, uses a weak chemical fixation during density gradient centrifugation to provide conformational stability and purify the sample, leading to a more homogenous population (Kastner et al., 2008; Stark, 2010).

Another concern is preferred orientations of the particles on the grid. Because the sample is confined to a thin layer of vitreous ice, it can interact with both the grid support and the air-water interfaces, leading to a bias in binding and therefore nonisotropic sampling of particle orientations (Stark, 2010). Noble et al. have recently shown that ~90% of particles on a typical cryo-EM grid prepared for SPA adsorb to the air–water interfaces, potentially causing preferred particle orientations, conformational changes in the protein, or protein denaturation (Noble et al., 2018). The use of continuous carbon support films to improve particle distribution may provide particular particle orientations, but it may also lead to even more significant orientation problems (Thompson et al., 2016). Self-assembled monolayers (Meyerson et al., 2014), poly-L-lysine (Chowdhury et al., 2015), and detergents (Zhang et al., 2011; Lyumkis et al., 2013), have all been used to reduce preferred orientation, but tend to be sample specific (Tan et al., 2017). The preferred orientation problem may also be addressed at the imaging level, by tilting the specimen during data collection (Tan et al., 2017). Better sampling in Fourier space can be achieved by tilting. However, at high tilts, there is a loss of high-spatial frequency information. Tilting creates a defocus gradient that must be accounted for and corrected. In addition, the ice thickness is increased relative to the electron beam, reducing contrast in the images (Tan et al., 2017).

Single particle cryo-EM of membrane proteins tends to be challenging because the proteins must be extracted from the membrane and solubilized in detergents, which may affect protein structure and function and reduce image contrast (Linke, 2009; Baker et al., 2015; Efremov et al., 2017). Amphipathic polymers called amphipols are a potential alternative to detergents. These are milder surfactants used to noncovalently bind the transmembrane portion of the protein, improving membrane protein solubility without affecting the contrast of the images. Amphipols have been used in the determination of several membrane protein structures (Flötenmeyer et al., 2007; Althoff et al., 2011; Cvetkov et al., 2011; Cao et al., 2013; Liao et al., 2013; Lu et al., 2014*a*; Wilkes et al., 2017). Another method of preparing membrane proteins for cryo-EM is the use of lipid nanodiscs (Frauenfeld et al., 2011; Efremov et al., 2015; Frauenfeld et al., 2016*a*; Gao et al., 2016; Gatsogiannis et al., 2016; Matthies et al., 2016; Shen et al., 2016; Jin et al., 2017). Nanodiscs consist of scaffold proteins surrounding a small lipid bilayer in which the protein of interest is reconstituted. This maintains a near native environment for the protein and provides additional particle size, which may be helpful for particle selection, although heterogeneity of the nanodisc may be a concern (Baker et al., 2015; Efremov et al., 2017).

Styrene maleic acid lipid particles (SMALPs) are an alternative to nanodiscs that do not require reconstitution of membrane proteins or detergents at any stage (Hardy et al., 2016). Styrene maleic acid (SMA) is an amphipathic co-polymer of alternating hydrophobic styrene and hydrophilic maleic acid units, which allows interaction with the membrane and provides solubility for the membrane protein. SMA is able to surround membrane proteins in their native lipids, producing native nanodisc SMALPs, which can then be purified and imaged (Hardy et al., 2016; Parmar et al., 2018). The structure of alternative complex III (ACIII) was recently solved to 3.4 Å using SMA nanodiscs (Sun et al., 2018). Yet another method for investigating membrane protein structure uses saposins in complex with lipids and the protein of interest (Salipro, saposin–lipid–protein) (Frauenfeld et al., 2016*b*; Lyons et al., 2017). Although the process requires the membrane protein to be solubilized in detergent, reconstitution into the Salipro complex is fast and the saposin scaffold can adapt to the size of the transmembrane region of the protein, providing a well-defined complex (Lyons et al., 2017).

Affinity grids are a new substrate designed to selectively adsorb particles on the EM grid by applying specific affinity between substrate and sample, allowing purification steps to be combined with grid preparation. The grid has a lipid monolayer containing Ni-nitrilotriacetic acid (Ni-NTA) lipids that can recruit polyhistidine tagged (His-tagged) proteins from cell extracts, reducing the required amount of protein and time for purification (Kelly et al., 2008). We have utilized affinity grids with His-tagged Protein A and anti-Env polyclonal antibody to study HIV CD84 virus-like particles (VLPs), resulting in less background and better control of particle density, as shown in Figure 2 (Kiss et al., 2014). An additional affinity capture method uses 2-dimensional (2D) streptavidin crystals on a lipid monolayer as a nanosupport applied to the EM grid (Wang et al., 2008). Biotinylated samples may then bind the streptavidin, improving particle concentration and distribution and reducing preferred particle orientations and the structural consequences of particles binding the carbon film or colliding with the air-water interface of the sample (Wang et al., 2008; Han et al., 2012*a*, 2016).

Further developments of the affinity grid include the use of a NTA-polyethylene glycol (PEG) based coating, which combines the anti-fouling properties of brush conformation methoxypolyethylene glycol (methoxy-PEG) with NTA ligands on flexible PEG spacers to prevent preferred orientation of the bound His-tagged proteins (Benjamin et al., 2016). Another example is a functionalized carbon film with covalently bound Ni-NTA, Protein G, or oligonucleotides to selectively recruit macromolecular complexes (Llaguno et al., 2014). In a simplified affinity grid method, called cryo-solid phase immune electron microscopy (SPIEM), antibodies or Protein A are applied directly to grids, eliminating the need to first apply a lipid monolayer (Yu et al., 2014, 2016*b*).

The use of the affinity capture system with silicon nitride (SiN) membrane support films has also shown promising improvements for sample preparation. The hydrophobicity of SiN supports interactions with the lipid tails of the Ni-NTA lipid monolayer, allowing for effective sample capture on the grid. Additionally, the membranes are flat, durable, and can be consistently manufactured, addressing the delicate and inconsistent nature of amorphous

https://doi.org/10.1017/S1431927618012382 Published online by Cambridge University Press

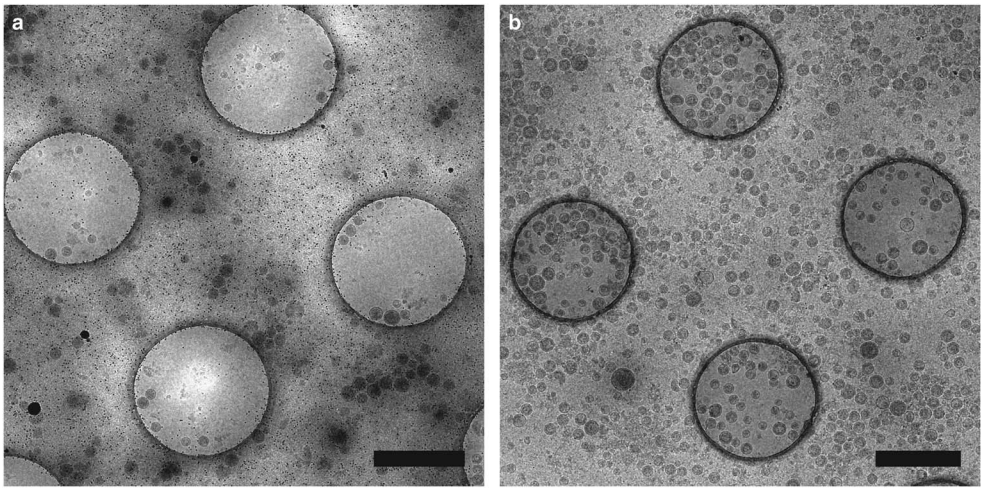

Figure 2. Affinity grid designed to selectively capture virus-like particles (VLPs). Cryo-electron microscopy images of HIV CD84 VLPs applied to an untreated grid (**a**) and a 20% Ni-NTA cryo-affinity grid with His-tagged Protein A and anti-Env polyclonal antibody (**b**). Use of the affinity capture method leads to increased VLP concentration and improved particle distribution on the grid. See Kiss et al. (2014) for experimental detail. Scale bar is 1 μm.

carbon supports (Tanner et al., 2013). Affinity grids combine purification steps with grid preparation, significantly reducing the time required to produce samples for cryo-EM imaging, and can be used for structure determination at high resolution. Yu et al. have recently used the method to determine the structure of a low concentration virus at 2.6 Å resolution (Yu et al., 2016*a*).

Traditional lacey, Quantifoil (Quantifoil Micro Tools, Jena, Germany), or C-flat (Protochips, Inc., Morrisville, NC, USA) EM grids are made of a metal scaffold (e.g., copper, nickel, or gold) and an amorphous carbon support with holes of various sizes, shapes, and distributions over which the sample is suspended in vitreous ice. Irradiation of amorphous carbon in the EM causes it to bend, however, leading to movement of the sample, often referred to as beam-induced motion, and therefore blurry images. Since the linear thermal expansion coefficient is much lower for carbon than for the metal support, the carbon film may also pucker at cryo-temperatures (Booy & Pawley, 1993). This can lead to poor imaging and the loss of information at high spatial frequencies. Several alternative substrates have been developed to address these deformations. Titanium–silicon metal glass films, a nanocrystalline silicon carbide substrate called Cryomesh (Proto-Chips, Inc.), and hydrogen-plasma treated graphene all decrease beam-induced motion, but do not completely eliminate it (Rhinow & Kuhlbrandt, 2008; Yoshioka et al., 2010; Russo & Passmore, 2014*a*). Ultrastable gold substrates, which consist of a gold foil across a gold mesh grid, are one of the most promising solutions. By using the same material for the support and grid, differential thermal contraction, and therefore puckering during cooling, is prevented and the high conductivity of gold nearly eliminates beam-induced motion, significantly improving image quality (Russo & Passmore, 2014*b*, 2016*a*, 2016*b*).

3D-DNA origami sample supports aim to address many of the current concerns for grid preparation. The sample particles are bound within a hollow support made up of double stranded DNA helices. This helps to control particle orientation, protects particles from the force of blotting with filter paper and from the air–liquid interface, and improves ice thickness consistency. The method was shown to be successful for the DNA binding protein p53, but will require more rigidity to precisely control particle orientation and will need to expand to be more widely applicable to various types of samples (Martin et al., 2016).

Protein scaffolds are also being used to determine the structures of monomeric proteins that would otherwise be too small for cryo-EM. Coscia et al. have designed a self-assembled symmetric protein scaffold with a small protein genetically fused, producing a large, rigid, and symmetric particle that is more amenable to cryo-EM, and solved the structure at subnanometer resolution (Coscia et al., 2016). Liu et al. have achieved near atomic resolution of a small protein called DARPin, which is rigidly fused to a self-assembled symmetric protein cage through terminal helices. The amino acid sequence of DARPin can be altered to tightly bind other small proteins, making it widely applicable (Liu et al., 2018).

Cryo-EM grid ice should ideally be only slightly thicker than the sample. Excess ice thickness should be avoided because it allows the particles within an image to be at different focal heights and contributes to noise in the images (Glaeser et al., 2016). Conventional blotting with filter paper often leads to inconsistent ice thickness and sample degradation due to the blotting force and it exposes the particles to an air–water interface of the sample. To address these problems, a "self-blotting" grid has been developed to generate reproducibly thin films of ice without the use of a filter paper blotting step (Razinkov et al., 2016; Wei et al., 2018). An ammonium persulfate and sodium hydroxide solution is applied to copper grids, supporting the growth of $Cu(OH)_2$ nanowires on the copper grid bars. The nanowires draw up excess liquid when the sample is applied to the grid, resulting in a thinly spread film of liquid on the grid that is then plunge frozen without the requirement of a blotting step. The self-blotting grids are used in conjunction with a newly designed freezing apparatus called the Spotiton (Jain et al., 2012; Dandey et al., 2018). This device uses a piezo controlled electric inkjet dispense head to deposit small volumes of sample at defined locations on the grid, which is then plunge frozen. Use of the self-blotting grid with the Spotiton results in thin films of uniform ice and the process is almost entirely automated, increasing the reproducibility and throughput of cryo-EM grid preparation (Jain et al., 2012; Razinkov et al., 2016; Dandey et al., 2018; Wei et al., 2018).

Another blotless freezing system called the cryoWriter allows real-time monitoring of the water thickness prior to vitrification (Arnold et al., 2017). A microcapillary is used to deposit a small sample volume (3–20 nanoliters) onto the grid. Depending on the volume applied, excess sample can either be recovered using the

https://doi.org/10.1017/S1431927618012382 Published online by Cambridge University Press

microcapillary or allowed to evaporate. The sample film is evaluated using a laser beam and photodetector and once the appropriate thickness is reached, the grid is plunge frozen. This system prevents the potentially damaging effects of filter paper blotting and uses significantly smaller volumes, allowing the investigation of low abundance samples.

Methods for time resolved imaging, to capture transient states of biological molecules, by mixing reaction components immediately before blotting have also seen recent improvements. This was initially achieved by applying one reaction component to the EM grid in the conventional pipetting and blotting manner to achieve a thin film, then spraying another component onto the film and rapidly freezing (Berriman & Unwin, 1994; Unwin, 1995; Walker et al., 1995; Walker et al., 1999; Berriman & Rosenthal, 2012; Unwin & Fujiyoshi, 2012). The reaction only proceeds where the components mix, however, potentially leading to heterogeneity in the sample across the grid. This problem was addressed by coupling a micromixer with a microsprayer, allowing external homogenous mixing of the reactants before spraying onto an EM grid and plunge freezing (Lu et al., 2009; Shaikh et al., 2014; Lu et al., 2014*b*). While this method allows the capture of dynamic processes for cryo-EM imaging, variability in ice thickness and coverage of the grid limits the regions suitable for data collection. The more recent development, by Feng et al., of a polydimethylsiloxane-based microsprayer allows the control of ice thickness through sprayer pressure and distance from the grid, and has the potential to provide time-resolved sample preparation by mixing reactants in a channel for specified amounts of time (Feng et al., 2017).

DIRECT ELECTRON DETECTORS

Low electron doses are necessary for the imaging of biological specimens in order to limit radiation damage of the sample. Cryo-EM images are therefore inherently noisy. Additionally, beam-induced motion of the sample leads to blurriness in the images. Both of these issues have been significantly improved by the development of direct electron detectors.

Several types of sensors may be used for the detection of electrons and the performance of the detector is extremely important for achieving high quality data. Detectors can be described by the detective quantum efficiency (DQE), a measure of signal produced from the sample and noise contributed to the image by the detector. A detector that contributes no noise to the image would have a DQE of 1.

Photographic film has historically been used to record cryo-EM images due to its large imaging area and high resolution. Its DQE is ~0.3–0.35 at half Nyquist frequency (McMullan et al., 2009*a*, 2016). The use of film can be labor intensive and time consuming, however, as it requires development and scanning into a digital format (Faruqi & Henderson, 2007; Binshtein & Ohi, 2015; Thompson et al., 2016). CCD cameras provide a much more automated mode of imaging, allowing for images to be immediately evaluated and for large data sets to be collected quickly. As the electrons hit the detector, a scintillator is used to induce the emission of photons which then hit the CCD. The photons are converted to electrical signals and an electrical charge accumulates. The charge is transferred between neighboring pixels and read out to form a digitized image (Faruqi, 1998; Sander et al., 2005; Thompson et al., 2016). The scintillator of a CCD camera produces electron and photon scattering, however, contributing additional noise to the images and leading to a DQE of ~0.07–0.1 at half Nyquist frequency, significantly inferior to that of photographic film (McMullan et al., 2009*a*, 2016).

Complementary metal-oxide semiconductor (CMOS) detectors are a digital alternative to CCD cameras that immediately convert charge to voltage within each pixel, so they can be operated at a high frame rate (Janesick & Putnam, 2003; Cheng et al., 2015; Faruqi et al., 2015). High frame rates provide the ability to fractionate the electron dose of an exposure over multiple frames. This allows the optimal use of electron dose in the image because one can compensate for the loss of high spatial frequency information as the dose accumulates. Frames can then be aligned before summing to correct for beam-induced motion and specimen drift in the image (McMullan et al., 2014).

CMOS-based direct detection devices (DDDs) have radiation hardened sensors that allow electrons to be recorded directly, rather than through a scintillator (McMullan et al., 2009*b*; Guerrini et al., 2011; Milazzo et al., 2011). This, along with back-thinning, which decreases backscattering of electrons, results in a considerable reduction of noise in the image compared with the noise from electron and photon scattering generated in the scintillator and fiber optics of a CCD (McMullan et al., 2009*c*). There are several types of DDDs that can be operated in various modes. In integration mode, charge is collected in each pixel, then integrated and read out. The DQE at half Nyquist in integration mode is ~0.4–0.6 (McMullan et al., 2016). In counting mode, the signal from each electron event is recorded and weighted the same, which reduces read noise and variability in electron signal. Operating in counting mode while using a high frame rate allows even higher DQEs to be achievable (Li et al., 2013*a*, 2013*b*). Some cameras may additionally be operated in what is called "super-resolution" mode, in which the electron events are sub-localized within the pixel, surpassing the Nyquist frequency limit (Li et al., 2013*a*, 2013*b*; Chiu et al., 2015).

The effects of motion correction can be seen in the image of coliphage BA14 collected on a Direct Electron DE-20 (Direct Electron, LP, San Diego, CA, USA) shown in Figure 3. The image was acquired at 12 frames per second with an exposure time of 5 s and then summed (Fig. 3a) or motion-corrected using scripts from Direct Electron, LP and summed (Fig. 3b). Blurring is significantly reduced by motion correction as shown in the images and power spectra. The ability to combine a high DQE with automation and the implementation of dose compensation and motion correction have led to a dramatic increase in the quality of cryo-EM data and the number of near-atomic to atomic resolution structures being determined (Lu et al., 2014*a*; Parent et al., 2014; Voorhees et al., 2014; Bartesaghi et al., 2015; Hesketh et al., 2015; von der Ecken et al., 2015; Merk et al., 2016).

Despite the improvements in DQE and signal-to-noise ratio provided by direct electron detectors, low contrast in cryo-EM images can still be problematic, particularly for small samples. Additional contrast enhancement, such as through the use of energy filters or phase plates, can be particularly useful in these cases.

PHASE PLATES

The contrast of unstained biological materials is inherently weak under low-electron dose cryo-EM imaging conditions. Contrast can be improved by defocusing of the objective lens, although this results in a reduction of the high spatial frequency components of the image, or with the use of an energy filter, which removes

https://doi.org/10.1017/S1431927618012382 Published online by Cambridge University Press

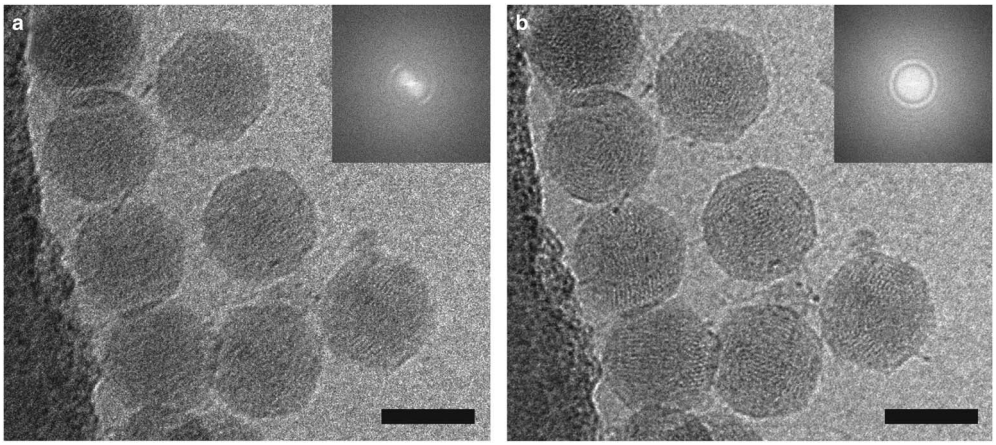

Figure 3. Motion correction of data recorded on a Direct Electron DE-20 direct electron detection device significantly improves image quality. Two-dimensional (2D) projection cryo-electron microscopy image of coliphage BA14 particles before (**a**) and after (**b**) motion correction using Direct Electron, LP scripts and the corresponding power spectra (insets). The image was recorded at a frame rate of 12 frames per second with an exposure time of 5 s. Scale bar is 50 nm.

inelastically scattered electrons thereby improving the signal-to-noise ratio (Langmore & Smith, 1992; Schroder, 1992). Another strategy for addressing low contrast in cryo-EM images is the use of phase plates. We have used two types of phase plates, the thin carbon-film Zernike-style phase plate and the hole-free carbon-film phase plate (HFPP), or Volta phase plate (VPP), although there are additional styles, such as electrostatic (Huang et al., 2006; Cambie et al., 2007; Majorovits et al., 2007; Schultheiss et al., 2010; Walter et al., 2012; Frindt et al., 2014) and magnetic phase plates (Edgcombe et al., 2012; Blackburn & Loudon, 2014).

Zernike phase contrast (ZPC) cryo-EM uses a thin carbon film with a small hole, produced by a focused ion beam (FIB), placed in the back focal plane (Danev & Nagayama, 2008; Nagayama & Danev, 2008; Murata et al., 2010; Schroder, 2015). Unscattered electrons pass through the hole while the scattered electrons go through the carbon film, shifting the phase of the unscattered electrons relative to the scattered electrons by $\pi/2$. This changes the contrast transfer function from a sine function to a cosine function (Nagayama, 2005) and significantly improves the contrast at low spatial frequencies. The images are acquired in focus, eliminating the loss in resolution due to defocusing. The higher contrast provided by phase plates improves image alignment, making it possible for fewer particles to be averaged to produce high resolution structures by SPA (Danev & Nagayama, 2008), and providing excellent results for cryo-ET (Danev et al., 2010; Murata et al., 2010; Guerrero-Ferreira et al., 2011; Fukuda & Nagayama, 2012; Dai et al., 2013). The use of ZPC cryo-EM can be challenging, however, due to a short lifespan, charging, difficulty keeping the phase plate aligned, and fringing artifacts in the images (Danev & Nagayama, 2001, 2010, 2011; Danev et al., 2009; Fukuda et al., 2009; Nagayama, 2011). Figure 4 and Supplementary Movie 1 illustrate the contrast provided by the Zernike-style phase plate in a tomogram of a *Caulobacter crescentus* cell infected with bacteriophage ϕCbK, as well as the fringing artifacts.

HFPP (or VPP) cryo-EM uses a homogenous carbon film in the back focal plane. Localized irradiation of the carbon film with the electron beam leads to a negative Volta potential, creating a phase shift at the position of the beam and increased contrast in the images (Danev et al., 2014). This form of phase plate has been shown to be more stable for data collection and does not introduce strong fringing artifacts (Danev & Nagayama, 2001, 2008, 2011; Danev et al., 2014; Danev & Baumeister, 2016; Khoshouei et al., 2016). It has recently been used to resolve extraordinary *in situ* detail via cryo-ET (Asano et al., 2015; Fukuda et al., 2015; Chlanda et al., 2016; Mahamid et al., 2016; Sharp et al., 2016; Khoshouei et al., 2017*a*) and to solve several high-resolution structures via SPA (Chua et al., 2016; Khoshouei et al., 2016, 2017*b*; Danev & Baumeister, 2017;). More recently, however, it has been possible to implement a slight defocus with this style of phase plate due to improvements in reconstruction software (Rohou & Grigorieff, 2015). This lessens the requirement for accuracy in focusing thus increasing the ease of use and the speed of data collection (Danev et al., 2017; Liang et al., 2017; Khoshouei et al., 2017*b*). Processing of defocused VPP data has been shown to be either equivalent or more robust than that of defocus phase contrast cryo-EM or in-focus VPP data, by enabling the generation of 3D reconstructions using fewer particles (von Loeffelholz et al., 2018). The use of phase plates continues to present practical challenges, however, and is generally limited to samples that are difficult to visualize without them. In Figure 5, we show 2D projection images of reovirus serotype 1 Lang (T1L) particles collected using HFPP and a slight defocus. The increased contrast allows the viral attachment fibers and released genome to be clearly resolved, without extreme fringing artifacts. Although both ZPC cryo-EM and HFPP cryo-EM provide significantly improved image contrast, the reduced fringing and relative ease of use of HFPP compared to ZPC phase plates will likely make them more widely applicable.

Cryo-CLEM

Correlative light and electron microscopy (CLEM or cryo-CLEM) is a technique that combines the spatiotemporal physiological information gained from fluorescence microscopy with the ever-higher resolution of structures from cryo-EM. The technique was developed in response to the absence of methods to unobtrusively label internal cell contents for cryo-EM and has been extremely useful for cellular cryo-ET studies in which localization of cellular components can be difficult in the EM. The fluorescence imaging can be done live or following vitrification of the cells to capture structures in their near-native state ("LM imaging" and "cryo-CLEM imaging," respectively, in Fig. 1) (Briegel et al., 2010). This

https://doi.org/10.1017/S1431927618012382 Published online by Cambridge University Press

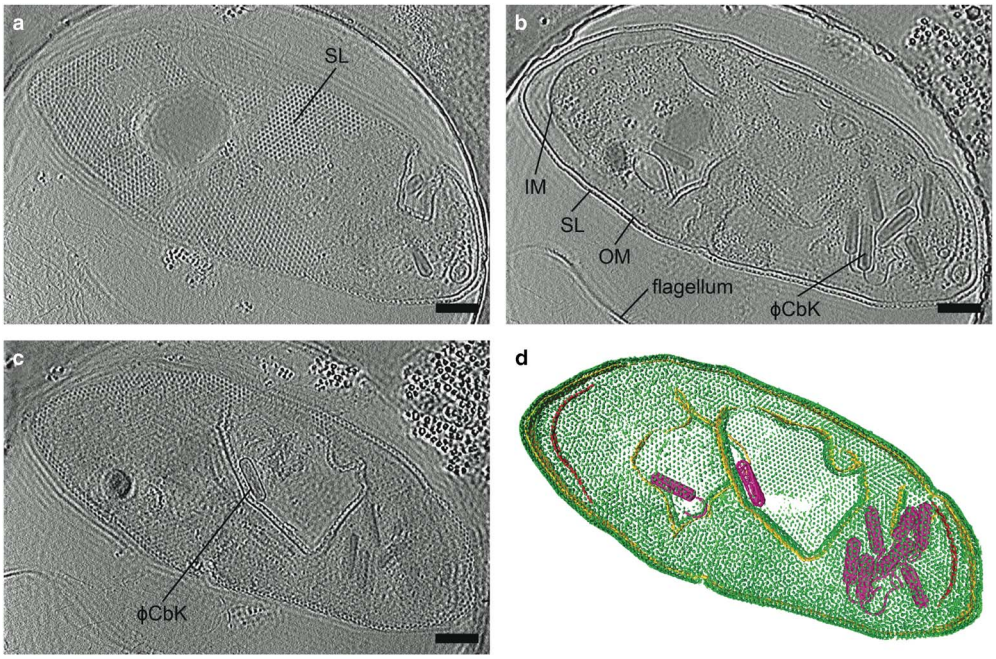

Figure 4. Zernike phase plate imaging of a phage-lysed bacterial cell provides contrast, revealing internal features. Cryo-electron tomography slices of ϕCbK phage-lysed *Caulobacter crescentus* cell using ZPC at zero defocus. **a:** A top slice of the tomogram illustrating the hexagonal surface layer (SL), (**b**) a central slice revealing newly assembled phages within the lysing cell, and (**c**) a central slice showing an assembled phage capsid in the process of genome packaging. Fringing artifacts are evident, particularly at the edge of the cell. **d:** Corresponding three-dimensional segmentation SL, green; OM, outer membrane, gold; IM, inner membrane, red; and ϕCbK, magenta. Scale bar is 200 nm.

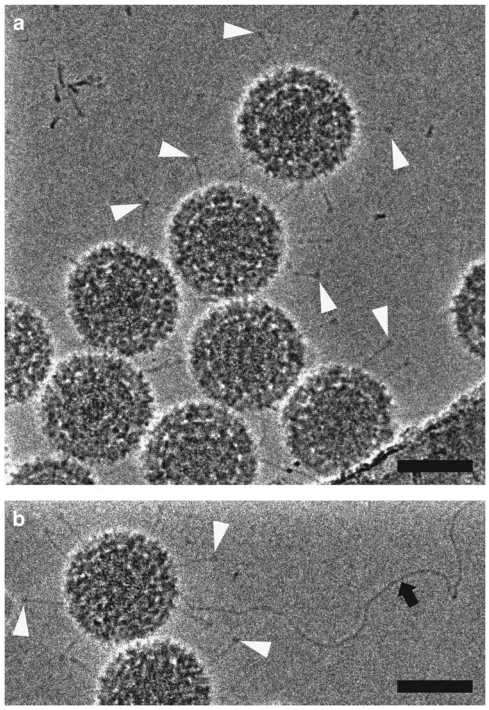

Figure 5. Hole-free phase plate (HFPP) imaging provides enhanced contrast without strong fringing artifacts. Cryo-electron microscopy images of reovirus T1L particles using HFPP slightly underfocus. **a,b**: Reovirus T1L particles displaying attachment fibers as indicated by white arrowheads. The black arrow points to a released viral genome in **b**. Scale bar is 50 nm.

is made possible by the introduction of cryo-cooled stages for the inverted or upright light microscope as well as the integrated light and EM (Sartori et al., 2007; Schwartz et al., 2007; Agronskaia et al., 2008; van Driel et al., 2009). Several advantages of cryo-fluorescence microscopy (cryo-fLM) include the absence of morphology-altering fixation, longer fluorophor lifespan (Moerner & Orrit, 1999; Schwartz et al., 2007; Le Gros et al., 2009), as well as a large field of view (Rigort et al., 2012; Bykov et al., 2016). This allows regions of interest to be identified quickly without subjecting the sample to a lengthy screening process in the EM, therefore preventing unnecessary irradiation of the sample before imaging. Relocating the region of interest in the EM is facilitated by the use of special finder-style EM grids or commercially available fiducials such as FluoSpheres or TetraSpeck beads (100–200 nm) that are both fluorescent and electron dense (Schellenberger et al., 2014; Schorb & Briggs, 2014). Marker-free alignment methods are also possible, as demonstrated by Anderson et al., in which the centers of the holes in the sample support are used for localization (Anderson et al., 2018).

Samples must be relatively thin in order to be penetrable by the electron beam (less than 1 μm) (Al-Amoudi et al., 2004), but must be even thinner for reliable 3D tomographic reconstruction (~250 nm). This is ideal for cryo-CLEM imaging of viruses (Schorb & Briggs, 2014), bacterial cells (Koning et al., 2014; Daley et al., 2016), or the thinnest regions of mammalian cells (van Driel et al., 2009; Zhang, 2013; Schellenberger et al., 2014; Carter et al., 2018). Additional techniques, such as FIB milling to produce thin lamella (Heymann et al., 2006; Marko et al., 2007; Rigort et al., 2010; Mahamid et al., 2015, 2016; Arnold et al., 2016; Chaikeeratisak et al., 2017), or cryo-ultramicrotomy (Al-Amoudi et al., 2004; Bouchet-Marquis & Fakan, 2009; Chlanda & Sachse, 2014; Kolovou et al., 2017), however, are required to access the interior of vitrified mammalian cells.

CLEM has been used to visualize the process of virus entry and exit from mammalian cells with great success. Using live-cell fluorescent imaging, cryo-fLM, and cryo-ET, Jun et al. has directly observed pseudo-typed HIV-1 virions with GFP-tagged HIV-1 Vpr interacting with HeLa cells at different time points after

https://doi.org/10.1017/S1431927618012382 Published online by Cambridge University Press

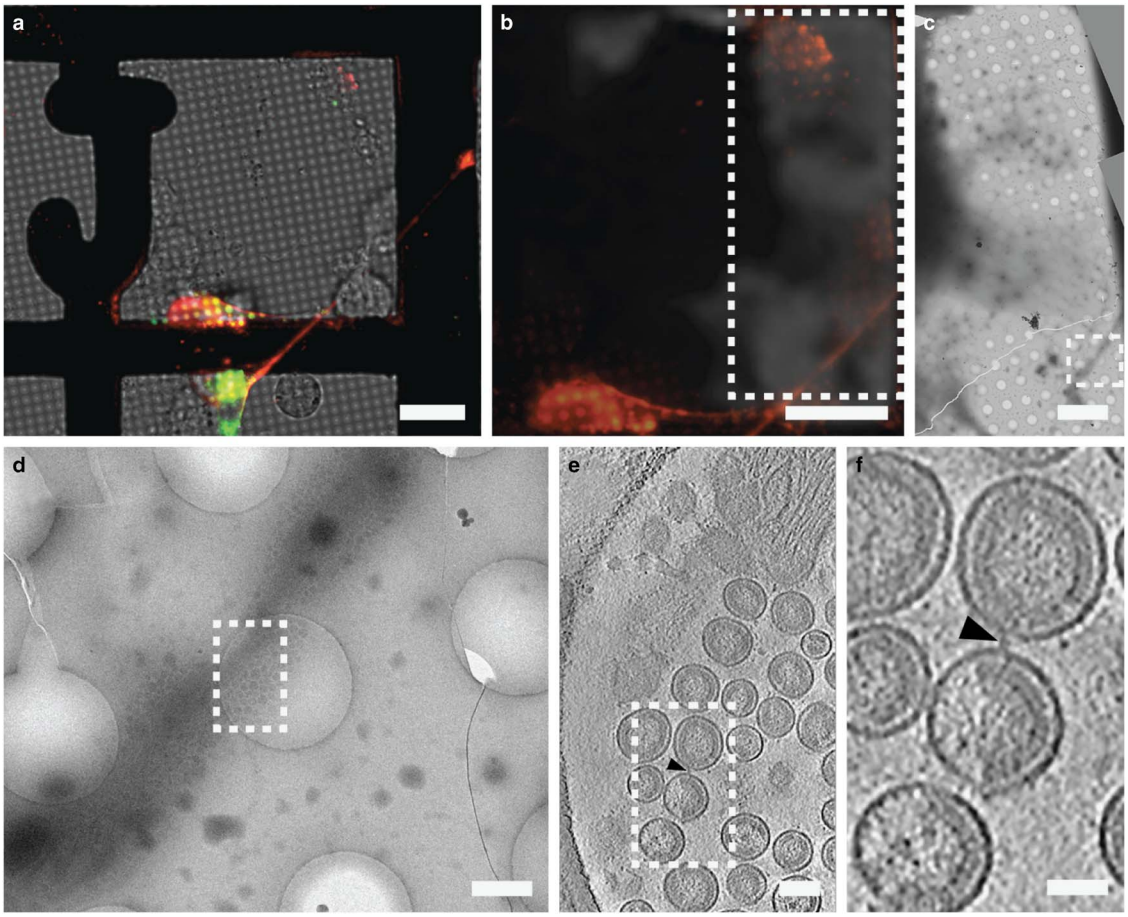

Figure 6. Correlative light and electron microscopy imaging of transfected mammalian cells provides multi-scale information. HT1080 cells grown on a gold London Finder grid and transfected with EGFP-tetherin (green) and mCherry-Gag (red) were imaged by live cell fluorescence microscopy (**a** and **b**), then plunge frozen and imaged by cryo-electron mincroscopy montaging (**c** and **d**), and cryo-electron tomography (**e** and **f**). The mCherry-Gag (red) signal in **a** and **b** corresponds to electron density of a thin cellular extension in **c** and **d**. The black arrowheads in **e** and **f** indicate a tether attaching two virus-like particles. Dashed boxes correspond to the enlarged image in the next panel. Adapted from Strauss et al. (2016). Scale bar: (**a** and **b**) 25 μm, (**c**) 10 μm, (**d**) 500 nm, (**e**) 100 nm, and (**f**) 50 nm.

infection (Jun et al., 2011). Ibiricu et al. used live-cell fluorescence microscopy followed by cryo-ET to identify time points and location of GFP-labeled herpes simplex virus undergoing axonal transport in primary neurons cultured directly on TEM grids (Ibiricu et al., 2011). To visualize virus after release, Strauss et al. used CLEM procedures to determine the arrangement of mCherry-Gag labeled HIV-1 particles anchored to cell plasma membranes via EGFP-tagged tetherin, a host cellular restriction factor that inhibits enveloped virus release, which can be seen in Figure 6 (Strauss et al., 2016). Hampton et al. further investigated these tethered particles using cryo-CLEM, as shown in Figure 7 (Hampton et al., 2017).

The latest improvements address many of the challenges associated with cryo-CLEM, such as contamination from atmospheric moisture during grid transfer steps, maintaining proper cryogenic temperatures during cryo-fLM imaging, and accurately correlating cryo-fLM and cryo-EM data. Schorb et al. have developed a system that optimizes grid transfer, stage stability, microscope optics, and software, establishing a comprehensive cryo-CLEM workflow (Schorb et al., 2017). Another system by Li et al. uses a high-vacuum chamber on the fluorescent microscope stage, decreasing contamination of the sample and allowing the objective lens to remain at room temperature. It has additionally been adapted to use a cryo-EM holder, reducing the number of grid transfer steps (Li et al., 2018). Future developments in CLEM will expand the use of cryo-super-resolution microscopy to localize specific proteins, further bridging the gap in resolution between light and electron microscopy (Chang et al., 2014; Kaufmann et al., 2014, 2016; Liu et al., 2015; Wolf et al., 2016).

CONCLUSIONS AND OUTLOOK

Since its development, cryo-EM has played an important role in structural biology and is contributing more and more with recent advances. New developments are broadening the cryo-EM spectrum from whole cells to peptides, allowing more biological questions of greater complexity to be answered and there is still room for improvement.

The timing and capturing of rare and specific events on the macromolecular and cellular levels is now possible using micro-sprayers and CLEM, respectively, for time-resolved imaging. Reproducibility in the sample preparation and grid preparation processes should continue to improve as grid-based purification methods and the development of vitrification devices such as the Spotiton and cryoWriter mature and expand. Beam-induced motion is being addressed both by the grid substrate and through the use of correction algorithms that utilize the high-frame rate of direct electron detectors.

https://doi.org/10.1017/S1431927618012382 Published online by Cambridge University Press

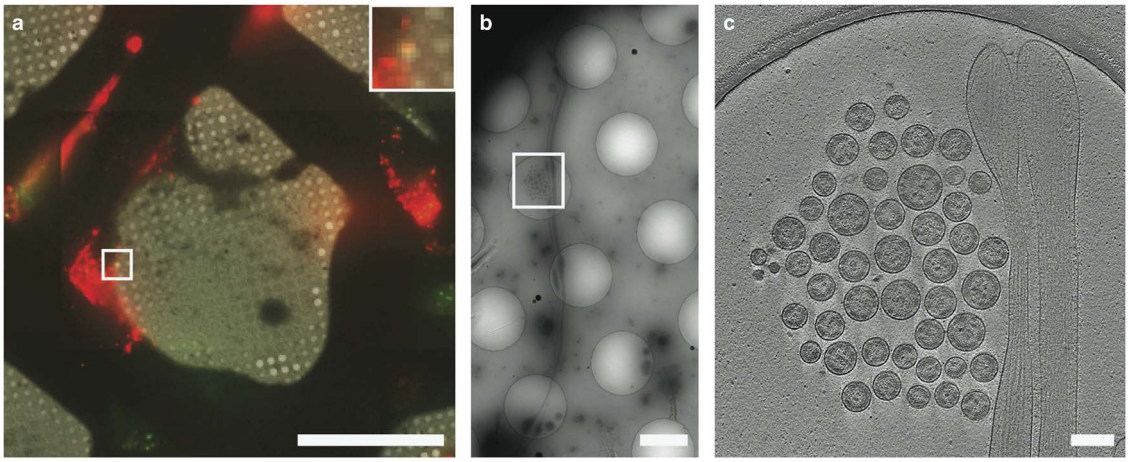

Figure 7. Cryo-correlative light and electron microscopy imaging of transfected mammalian cells. HT1080 cells transfected with EGFP-tetherin (green) and mCherry-Gag (red) imaged by cryo-fluorescence microscopy (**a**), cryo-electron mincroscopy montaging (**b**), and cryo-electron tomography (**c**). Dashed boxes correspond to the enlarged image in the next panel. The yellow signal in **a** (inset) indicates colocalization of EGFP-tetherin (green) and mCherry-Gag (red) signal and corresponds to a cluster of HIV-1 virus-like particles tethered to a cellular extension in **b** and **c**. Adapted from Hampton et al. (2017). Scale bar: (**a**) 50 μm, inset is 3×, (**b**) 2 μm, (**c**) 200 nm.

Advances in electron detection over the past several years have provided remarkable improvements for cryo-EM data collection and quality. Further increasing frame rates, the use of counting mode on all systems, and increased pixel sizes will provide even higher DQEs and super resolution mode should allow direct electron detectors to be used beyond Nyquist frequency (McMullan et al., 2016).

While phase plates have shown extraordinary promise for cryo-EM, there are still improvements that can be made. Usage is generally limited to those with expertise (Danev & Nagayama, 2008; Glaeser et al., 2013; Subramaniam et al., 2016) and takes a considerable amount of time, so workflow development will be incredibly important for more widespread implementation. Higher reproducibility in the manufacture of phase plates and methods for evaluating phase plate quality during use will also prove to be useful. Phase plates should allow increasingly higher resolution structural work, particularly for small samples, and for entire data sets to be collected more quickly since fewer images will be required.

As CLEM continues to develop, labeling strategies that are retained between live cell and cryo-EM imaging will allow more and more complex biological questions to be addressed and simultaneously fluorescent and electron-dense markers will aid in more precise correlation between light and electron microscopy. Combining cryo-FIB milling of cryo-samples with cryo-CLEM will provide a method for thicker specimens to be investigated and improvements to sample stability between steps of the workflow will help the process become more user-friendly.

The recent developments in cryo-EM imaging, along with improvements in image processing, have allowed tremendous growth in the field over the last few years. We expect this expansion to continue, with cryo-EM providing structures to higher resolutions and answers to increasingly intricate biological questions.

Supplementary material. To view supplementary material for this article, please visit https://doi.org/10.1017/S1431927618012382

Acknowledgments. The authors acknowledge the Robert P. Apkarian Integrated Electron Microscopy Core of Emory University for microscopy services and support. The authors also thank Prof. Xuemin Chen for the HIV-1 VLPs, Prof. Bernardo Mainou for the reovirus T1L preparation, and Prof. Ian Molineux for providing us with coliphage BA14. This work was supported in part by Emory University, Children's Healthcare of Atlanta, and the Georgia Research Alliance to E.R.W.; the Center for AIDS Research at Emory University (P30 AI050409); the James B. Pendleton Charitable Trust to E.R.W.; public health service grants R01GM104540, R01GM114561, R21AI101775, R01GM104540-03S1 to E.R.W. from the NIH, and NSF grant 0923395 to E.R.W. Public health service grant F32GM112517 to J.D.S. from the NIH. Reovirus data collection at Florida State University was made possible by NIH grants S10 OD018142-01, S10 RR025080-01, and U24 GM116788 to K. A. T.

References

Adrian M, Dubochet J, Lepault J and Mcdowall AW (1984) Cryo-electron microscopy of viruses. *Nature* **308**(5954), 32–36.

Agafonov DE, Kastner B, Dybkov O, Hofele RV, Liu WT, Urlaub H, Luhrmann R and Stark H (2016) Molecular architecture of the human U4/U6.U5 tri-snRNP. *Science* **351**(6280), 1416–1420.

Agronskaia AV, Valentijn JA, van Driel LF, Schneijdenberg CT, Humbel BM, van Bergen en Henegouwen PM, Verkleij AJ, Koster AJ and Gerritsen HC (2008) Integrated fluorescence and transmission electron microscopy. *J Struct Biol* **164**(2), 183–189.

Al-Amoudi A, Chang JJ, Leforestier A, McDowall A, Salamin LM, Norlen LP, Richter K, Blanc NS, Studer D and Dubochet J (2004) Cryo-electron microscopy of vitreous sections. *EMBO J* **23**(18), 3583–3588.

Althoff T, Mills DJ, Popot J-L and Kühlbrandt W (2011) Arrangement of electron transport chain components in bovine mitochondrial supercomplex I(1)III(2)IV(1). *EMBO J* **30**(22), 4652–4664.

Anderson KL, Page C, Swift MF, Hanein D and Volkmann N (2018) Marker-free method for accurate alignment between correlated light, cryo-light, and electron cryo-microscopy data using sample support features. *J Struct Biol* **201**(1), 46–51.

Arnold J, Mahamid J, Lucic V, de Marco A, Fernandez J-J, Laugks T, Mayer T, Hyman, Anthony A, Baumeister W and Plitzko JM (2016) Site-specific cryo-focused ion beam sample preparation guided by 3D correlative microscopy. *Biophys J* **110**(4), 860–869.

Arnold SA, Albiez S, Bieri A, Syntychaki A, Adaixo R, McLeod RA, Goldie KN, Stahlberg H and Braun T (2017) Blotting-free and lossless cryo-electron microscopy grid preparation from nanoliter-sized protein samples and single-cell extracts. *J Struct Biol* **197**(3), 220–226.

Asano S, Fukuda Y, Beck F, Aufderheide A, Forster F, Danev R and Baumeister W (2015) Proteasomes. A molecular census of 26S proteasomes in intact neurons. *Science* **347**(6220), 439–442.

Bai X-C, McMullan G and Scheres SHW (2015) How cryo-EM is revolutionizing structural biology. *Trends Biochem Sci* **40**(1), 49–57.

Baker MR, Fan G and Serysheva II (2015) Single-particle cryo-EM of the ryanodine receptor channel in an aqueous environment. *Eur J Transl Myol* **25**(1), 35–48.

Bartesaghi A, Merk A, Banerjee S, Matthies D, Wu X, Milne JL and Subramaniam S (2015) 2.2 Å resolution cryo-EM structure of beta-galactosidase in complex with a cell-permeant inhibitor. *Science* **348**(6239), 1147–1151.

Benjamin CJ, Wright KJ, Hyun SH, Krynski K, Yu G, Bajaj R, Guo F, Stauffacher CV, Jiang W and Thompson DH (2016) Nonfouling NTA-PEG-based TEM grid coatings for selective capture of histidine-tagged protein targets from cell lysates. *Langmuir* **32**(2), 551–559.

Berriman J and Unwin N (1994) Analysis of transient structures by cryo-microscopy combined with rapid mixing of spray droplets. *Ultramicroscopy* **56**(4), 241–252.

Berriman JA and Rosenthal PB (2012) Paraxial charge compensator for electron cryomicroscopy. *Ultramicroscopy* **116**, 106–114.

Bertram K, Agafonov DE, Liu WT, Dybkov O, Will CL, Hartmuth K, Urlaub H, Kastner B, Stark H and Luhrmann R (2017) Cryo-EM structure of a human spliceosome activated for step 2 of splicing. *Nature* **542**(7641), 318–323.

Binshtein E and Ohi MD (2015) Cryo-electron microscopy and the amazing race to atomic resolution. *Biochemistry* **54**(20), 3133–3141.

Blackburn AM and Loudon JC (2014) Vortex beam production and contrast enhancement from a magnetic spiral phase plate. *Ultramicroscopy* **136**, 127–143.

Booy FP and Pawley JB (1993) Cryo-crinkling: What happens to carbon films on copper grids at low temperature. *Ultramicroscopy* **48**(3), 273–280.

Bouchet-Marquis C and Fakan S (2009) Cryoelectron microscopy of vitreous sections: A step further towards the native state. *Methods Mol Biol* **464**, 425–439.

Briegel A, Chen S, Koster AJ, Plitzko JM, Schwartz CL and Jensen GJ (2010) Chapter Thirteen – Correlated light and electron cryo-microscopy. In: *Methods in Enzymology*, Jensen GJ (Ed.), pp. 317–341. Oxford, UK: Academic Press.

Brilot AF, Chen JZ, Cheng A, Pan J, Harrison SC, Potter CS, Carragher B, Henderson R and Grigorieff N (2012) Beam-induced motion of vitrified specimen on holey carbon film. *J Struct Biol* **177**(3), 630–637.

Bykov YS, Cortese M, Briggs JAG and Bartenschlager R (2016) Correlative light and electron microscopy methods for the study of virus–cell interactions. *FEBS Lett* **590**(13), 1877–1895.

Cambie R, Downing KH, Typke D, Glaeser RM and Jin J (2007) Design of a microfabricated, two-electrode phase-contrast element suitable for electron microscopy. *Ultramicroscopy* **107**(4–5), 329–339.

Cao E, Liao M, Cheng Y and Julius D (2013) TRPV1 structures in distinct conformations reveal mechanisms of activation. *Nature* **504**(7478), 113–118.

Carter SD, Mageswaran SK, Farino ZJ, Mamede JI, Oikonomou CM, Hope TJ, Freyberg Z and Jensen GJ (2018) Distinguishing signal from autofluorescence in cryogenic correlated light and electron microscopy of mammalian cells. *J Struct Biol* **201**(1), 15–25.

Chaikeeratisak V, Nguyen K, Khanna K, Brilot AF, Erb ML, Coker JK, Vavilina A, Newton GL, Buschauer R, Pogliano K, Villa E, Agard DA and Pogliano J (2017) Assembly of a nucleus-like structure during viral replication in bacteria. *Science* **355**(6321), 194–197.

Chang Y-W, Chen S, Tocheva EI, Treuner-Lange A, Löbach S, Søgaard-Andersen L and Jensen GJ (2014) Correlated cryogenic photoactivated localization microscopy and cryo-electron tomography. *Nat Methods* **11**, 737.

Cheng Y, Grigorieff N, Penczek PA and Walz T (2015) A primer to single-particle cryo-electron microscopy. *Cell* **161**(3), 438–449.

Chiu P-L, Li X, Li Z, Beckett B, Brilot AF, Grigorieff N, Agard DA, Cheng Y and Walz T (2015) Evaluation of super-resolution performance of the K2 electron-counting camera using 2D crystals of aquaporin-0. *J Struct Biol* **192**(2), 163–173.

Chlanda P, Mekhedov E, Waters H, Schwartz CL, Fischer ER, Ryham RJ, Cohen FS, Blank PS and Zimmerberg J (2016) The hemifusion structure induced by influenza virus haemagglutinin is determined by physical properties of the target membranes. *Nat Microbiol* **1**(6), 16050.

Chlanda P and Sachse M (2014) Cryo-electron microscopy of vitreous sections. *Methods Mol Biol* **1117**, 193–214.

Chowdhury S, Ketcham SA, Schroer TA and Lander GC (2015) Structural organization of the dynein-dynactin complex bound to microtubules. *Nat Struct Mol Biol* **22**(4), 345–347.

Chua EY, Vogirala VK, Inian O, Wong AS, Nordenskiold L, Plitzko JM, Danev R and Sandin S (2016) 3.9 Å structure of the nucleosome core particle determined by phase-plate cryo-EM. *Nucleic Acids Res* **44**(17), 8013–8019.

Coscia F, Estrozi LF, Hans F, Malet H, Noirclerc-Savoye M, Schoehn G and Petosa C (2016) Fusion to a homo-oligomeric scaffold allows cryo-EM analysis of a small protein. *Sci Rep* **6**, 30909.

Cvetkov TL, Huynh KW, Cohen MR and Moiseenkova-Bell VY (2011) Molecular architecture and subunit organization of TRPA1 ion channel revealed by electron microscopy. *J Biol Chem* **286**(44), 38168–38176.

Dahl R and Staehelin LA (1989) High-pressure freezing for the preservation of biological structure: Theory and practice. *J Electron Microsc Tech* **13**(3), 165–174.

Dai W, Fu C, Raytcheva D, Flanagan J, Khant HA, Liu X, Rochat RH, Haase-Pettingell C, Piret J, Ludtke SJ, Nagayama K, Schmid MF, King JA and Chiu W (2013) Visualizing virus assembly intermediates inside marine cyanobacteria. *Nature* **502**(7473), 707–710.

Daley DO, Skoglund U and Söderström B (2016) FtsZ does not initiate membrane constriction at the onset of division. *Sci Rep* **6**, 33138.

Dandey VP, Wei H, Zhang Z, Tan YZ, Acharya P, Eng ET, Rice WJ, Kahn PA, Potter CS and Carragher B (2018) Spotiton: New features and applications. *J Struct Biol* **202**(2), 161–169.

Danev R and Baumeister W (2016) Cryo-EM single particle analysis with the Volta phase plate. *eLife* **5**, e13046.

Danev R and Baumeister W (2017) Expanding the boundaries of cryo-EM with phase plates. *Curr Opin Struct Biol* **46**, 87–94.

Danev R, Buijsse B, Khoshouei M, Plitzko JM and Baumeister W (2014) Volta potential phase plate for in-focus phase contrast transmission electron microscopy. *Proc Natl Acad Sci USA* **111**(44), 15635–15640.

Danev R, Glaeser RM and Nagayama K (2009) Practical factors affecting the performance of a thin-film phase plate for transmission electron microscopy. *Ultramicroscopy* **109**(4), 312–325.

Danev R, Kanamaru S, Marko M and Nagayama K (2010) Zernike phase contrast cryo-electron tomography. *J Struct Biol* **171**(2), 174–181.

Danev R and Nagayama K (2001) Transmission electron microscopy with Zernike phase plate. *Ultramicroscopy* **88**(4), 243–252.

Danev R and Nagayama K (2008) Single particle analysis based on Zernike phase contrast transmission electron microscopy. *J Struct Biol* **161**(2), 211–218.

Danev R and Nagayama K (2010) Phase plates for transmission electron microscopy. *Methods Enzymol* **481**, 343–369.

Danev R and Nagayama K (2011) Optimizing the phase shift and the cut-on periodicity of phase plates for TEM. *Ultramicroscopy* **111**(8), 1305–1315.

Danev R, Tegunov D and Baumeister W (2017) Using the Volta phase plate with defocus for cryo-EM single particle analysis. *eLife* **6**, e23006.

Doerr A (2015) Single-particle cryo-electron microscopy. *Nat Methods* **13**, 23.

Dubochet J (1995) High-pressure freezing for cryoelectron microscopy. *Trends Cell Biol* **5**(9), 366–368.

Dubochet J, Adrian M, Chang JJ, Homo JC, Lepault J, McDowall AW and Schultz P (1988) Cryo-electron microscopy of vitrified specimens. *Q Rev Biophys* **21**(2), 129–228.

Dubochet J, McDowall AW, Menge B, Schmid EN and Lickfeld KG (1983) Electron microscopy of frozen-hydrated bacteria. *J Bacteriol* **155**(1), 381–390.

Edgcombe CJ, Ionescu A, Loudon JC, Blackburn AM, Kurebayashi H and Barnes CHW (2012) Characterisation of ferromagnetic rings for Zernike phase plates using the Aharonov–Bohm effect. *Ultramicroscopy* **120**, 78–85.

Efremov RG, Gatsogiannis C and Raunser S (2017) Chapter One – Lipid nanodiscs as a tool for high-resolution structure determination of membrane proteins by single-particle cryo-EM. In: *Methods in Enzymology*, Ziegler, C (Ed.), pp. 1–30. Oxford, UK: Academic Press.

Efremov RG, Leitner A, Aebersold R and Raunser S (2015) Architecture and conformational switch mechanism of the ryanodine receptor. *Nature* **517**, 39.

https://doi.org/10.1017/S1431927618012382 Published online by Cambridge University Press

Faruqi AR (1998) Design principles and applications of a cooled CCD camera for electron microscopy. *Adv Exp Med Biol* **453**, 63–72.

Faruqi AR and Henderson R (2007) Electronic detectors for electron microscopy. *Curr Opin Struct Biol* **17**(5), 549–555.

Faruqi AR, Henderson R and McMullan G (2015) Chapter Two – Progress and development of direct detectors for electron cryomicroscopy. In: *Advances in Imaging and Electron Physics*, Hawkes PW (Ed.), pp. 103–141. Oxford, UK: Elsevier.

Feng X, Fu Z, Kaledhonkar S, Jia Y, Shah B, Jin A, Liu Z, Sun M, Chen B, Grassucci RA, Ren Y, Jiang H, Frank J and Lin Q (2017) A fast and effective microfluidic spraying-plunging method for high-resolution single-particle cryo-EM. *Structure* **25**(4), 663–670.e663.

Fernandez-Leiro R and Scheres SHW (2016) Unravelling biological macromolecules with cryo-electron microscopy. *Nature* **537**, 339.

Fiedorczuk K, Letts JA, Degliesposti G, Kaszuba K, Skehel M and Sazanov LA (2016) Atomic structure of the entire mammalian mitochondrial complex I. *Nature* **538**(7625), 406–410.

Flötenmeyer M, Weiss H, Tribet C, Popot J-L and Leonard K (2007) The use of amphipathic polymers for cryo electron microscopy of NADH: ubiquinone oxidoreductase (complex I). *J Microsc* **227**(3), 229–235.

Frank J (2017) Advances in the field of single-particle cryo-electron microscopy over the last decade. *Nat Protoc* **12**, 209.

Frauenfeld J, Gumbart J, van der Sluis EO, Funes S, Gartmann M, Beatrix B, Mielke T, Berninghausen O, Becker T, Schulten K and Beckmann R (2011) Cryo–EM structure of the ribosome–SecYE complex in the membrane environment. *Nat Struct Mol Biol* **18**(5), 614–621.

Frauenfeld J, Löving R, Armache J-P, Sonnen A, Guettou F, Moberg P, Zhu L, Jegerschöld C, Flayhan A, Briggs JAG, Garoff H, Löw C, Cheng Y and Nordlund P (2016*a*) A novel lipoprotein nanoparticle system for membrane proteins. *Nat Methods* **13**(4), 345–351.

Frauenfeld J, Löving R, Armache J-P, Sonnen AFP, Guettou F, Moberg P, Zhu L, Jegerschöld C, Flayhan A, Briggs JAG, Garoff H, Löw C, Cheng Y and Nordlund P (2016*b*) A saposin-lipoprotein nanoparticle system for membrane proteins. *Nat Methods* **13**, 345.

Frindt N, Oster M, Hettler S, Gamm B, Dieterle L, Kowalsky W, Gerthsen D and Schröder RR (2014) In-focus electrostatic Zach phase plate imaging for transmission electron microscopy with tunable phase contrast of frozen hydrated biological samples. *Microsc Microanal* **20**(1), 175–183.

Fukuda Y, Fukazawa Y, Danev R, Shigemoto R and Nagayama K (2009) Tuning of the Zernike phase-plate for visualization of detailed ultra-structure in complex biological specimens. *J Struct Biol* **168**(3), 476–484.

Fukuda Y, Laugks U, Lucic V, Baumeister W and Danev R (2015) Electron cryotomography of vitrified cells with a Volta phase plate. *J Struct Biol* **190** (2), 143–154.

Fukuda Y and Nagayama K (2012) Zernike phase contrast cryo-electron tomography of whole mounted frozen cells. *J Struct Biol* **177**(2), 484–489.

Gao Y, Cao E, Julius D and Cheng Y (2016) TRPV1 structures in nanodiscs reveal mechanisms of ligand and lipid action. *Nature* **534**, 347.

Gatsogiannis C, Merino F, Prumbaum D, Roderer D, Leidreiter F, Meusch D and Raunser S (2016) Membrane insertion of a Tc toxin in near-atomic detail. *Nat Struct Mol Biol* **23**, 884.

Glaeser RM, Han BG, Csencsits R, Killilea A, Pulk A and Cate JH (2016) Factors that influence the formation and stability of thin, cryo-EM specimens. *Biophys J* **110**(4), 749–755.

Glaeser RM, McMullan G, Faruqi AR and Henderson R (2011) Images of paraffin monolayer crystals with perfect contrast: Minimization of beam-induced specimen motion. *Ultramicroscopy* **111**(2), 90–100.

Glaeser RM, Sassolini S, Cambie R, Jin J, Cabrini S, Schmid AK, Danev R, Buijsse B, Csencsits R, Downing KH, Larson DM, Typke D and Han BG (2013) Minimizing electrostatic charging of an aperture used to produce in-focus phase contrast in the TEM. *Ultramicroscopy* **135**, 6–15.

Grabenbauer M, Han HM and Huebinger J (2014) Cryo-fixation by self-pressurized rapid freezing. *Methods Mol Biol* **1117**, 173–191.

Guerrero-Ferreira RC, Viollier PH, Ely B, Poindexter JS, Georgieva M, Jensen GJ and Wright ER (2011) Alternative mechanism for bacteriophage adsorption to the motile bacterium *Caulobacter crescentus*. *Proc Natl Acad Sci U S A* **108**(24), 9963.

Guerrini N, Turchetta R, Hoften GV, Henderson R, McMullan G and Faruqi AR (2011) A high frame rate, 16 million pixels, radiation hard CMOS sensor. *J Instrum* **6**(3), C03003.

Guo F and Jiang W (2014) Single particle cryo-electron microscopy and 3-D reconstruction of viruses. *Methods Mol Biol* **1117**, 401–443.

Hampton CM, Strauss JD, Ke Z, Dillard RS, Hammonds JE, Alonas E, Desai TM, Marin M, Storms RE, Leon F, Melikyan GB, Santangelo PJ, Spearman PW and Wright ER (2017) Correlated fluorescence microscopy and cryo-electron tomography of virus-infected or transfected mammalian cells. *Nat Protoc* **12**(1), 150–167.

Han B-G, Watson Z, Kang H, Pulk A, Downing KH, Cate J and Glaeser RM (2016) Long shelf-life streptavidin support-films suitable for electron microscopy of biological macromolecules. *J Struct Biol* **195**(2), 238–244.

Han BG, Walton RW, Song A, Hwu P, Stubbs MT, Yannone SM, Arbelaez P, Dong M and Glaeser RM (2012*a*) Electron microscopy of biotinylated protein complexes bound to streptavidin monolayer crystals. *J Struct Biol* **180**(1), 249–253.

Han H-M, Huebinger J and Grabenbauer M (2012*b*) Self-pressurized rapid freezing (SPRF) as a simple fixation method for cryo-electron microscopy of vitreous sections. *J Struct Biol* **178**(2), 84–87.

Hardy D, Bill RM, Jawhari A and Rothnie AJ (2016) Overcoming bottlenecks in the membrane protein structural biology pipeline. *Biochem Soc Trans* **44**(3), 838.

Hesketh EL, Meshcheriakova Y, Dent KC, Saxena P, Thompson RF, Cockburn JJ, Lomonossoff GP and Ranson NA (2015) Mechanisms of assembly and genome packaging in an RNA virus revealed by high-resolution cryo-EM. *Nat Commun* **6**, 10113.

Hewat EA and Neumann E (2002) Characterization of the performance of a 200-kV field emission gun for cryo-electron microscopy of biological molecules. *J Struct Biol* **139**(1), 60–64.

Heymann JA, Hayles M, Gestmann I, Giannuzzi LA, Lich B and Subramaniam S (2006) Site-specific 3D imaging of cells and tissues with a dual beam microscope. *J Struct Biol* **155**(1), 63–73.

Huang SH, Wang WJ, Chang CS, Hwu YK, Tseng FG, Kai JJ and Chen FR (2006) The fabrication and application of Zernike electrostatic phase plate. *J Electron Microsc (Tokyo)* **55**(6), 273–280.

Ibiricu I, Huiskonen JT, Dohner K, Bradke F, Sodeik B and Grunewald K (2011) Cryo electron tomography of herpes simplex virus during axonal transport and secondary envelopment in primary neurons. *PLoS Pathog* **7** (12), e1002406.

Jain T, Sheehan P, Crum J, Carragher B and Potter CS (2012) Spotiton: A prototype for an integrated inkjet dispense and vitrification system for cryo-TEM. *J Struct Biol* **179**(1), 68–75.

Janesick J and Putnam G (2003) Developments and applications of high-performance CCD and CMOS imaging arrays. *Annu Rev Nucl Particle Sci* **53**(1), 263–300.

Jin P, Bulkley D, Guo Y, Zhang W, Guo Z, Huynh W, Wu S, Meltzer S, Cheng T, Jan LY, Jan Y-N and Cheng Y (2017) Cryo-EM structure of the mechanotransduction channel NOMPC. *Nature* **547**(7661), 118–122.

Jun S, Ke D, Debiec K, Zhao G, Meng X, Ambrose Z, Gibson GA, Watkins SC and Zhang P (2011) Direct visualization of HIV-1 with correlative live-cell microscopy and cryo-electron tomography. *Structure* **19**(11), 1573–1581.

Kastner B, Fischer N, Golas MM, Sander B, Dube P, Boehringer D, Hartmuth K, Deckert J, Hauer F, Wolf E, Uchtenhagen H, Urlaub H, Herzog F, Peters JM, Poerschke D, Luhrmann R and Stark H (2008) GraFix: Sample preparation for single-particle electron cryomicroscopy. *Nat Methods* **5**(1), 53–55.

Kaufmann R, Hagen C and Grünewald K (2016) Super-resolution fluorescence microscopy of cryo-immobilized samples. In: *European Microscopy Congress 2016: Proceedings*, p. 1017. Weinheim, Germany: Wiley-VCH Verlag GmbH & Co. KGaA.

Kaufmann R, Schellenberger P, Seiradake E, Dobbie IM, Jones EY, Davis I, Hagen C and Grünewald K (2014) Super-resolution microscopy using standard fluorescent proteins in intact cells under cryo-conditions. *Nano Lett* **14**(7), 4171–4175.

https://doi.org/10.1017/S1431927618012382 Published online by Cambridge University Press

Kelly DF, **Abeyrathne PD**, **Dukovski D and Walz T** (2008) The affinity grid: A pre-fabricated EM grid for monolayer purification. *J Mol Biol* **382**(2), 423–433.

Khoshouei M, **Pfeffer S**, **Baumeister W**, **Forster F and Danev R** (2017*a*) Subtomogram analysis using the Volta phase plate. *J Struct Biol* **197**(2), 94–101.

Khoshouei M, **Radjainia M**, **Baumeister W and Danev R** (2017*b*) Cryo-EM structure of haemoglobin at 3.2 Å determined with the Volta phase plate. *Nat Commun* **8**, 16099.

Khoshouei M, **Radjainia M**, **Phillips AJ**, **Gerrard JA**, **Mitra AK**, **Plitzko JM**, **Baumeister W and Danev R** (2016) Volta phase plate cryo-EM of the small protein complex Prx3. *Nat Commun* **7**, 10534.

Kiss G, **Chen X**, **Brindley MA**, **Campbell P**, **Afonso CL**, **Ke Z**, **Holl JM**, **Guerrero-Ferreira RC**, **Byrd-Leotis LA**, **Steel J**, **Steinhauer DA**, **Plemper RK**, **Kelly DF**, **Spearman PW and Wright ER** (2014) Capturing enveloped viruses on affinity grids for downstream cryo-electron microscopy applications. *Microsc Microanal* **20**(1), 164–174.

Kolovou A, **Schorb M**, **Tarafder A**, **Sachse C**, **Schwab Y and Santarella-Mellwig R** (2017) A new method for cryo-sectioning cell monolayers using a correlative workflow. *Methods Cell Biol* **140**, 85–103.

Koning RI, **Celler K**, **Willemse J**, **Bos E**, **van Wezel GP and Koster AJ** (2014) Chapter 10 – Correlative cryo-fluorescence light microscopy and cryo-electron tomography of streptomyces. In: *Methods in Cell Biology*, Müller-Reichert T and Verkade P (Eds.), pp. 217–239. Oxford, UK: Academic Press.

Kosinski J, **Mosalaganti S**, **von Appen A**, **Teimer R**, **DiGuilio AL**, **Wan W**, **Bui KH**, **Hagen WJH**, **Briggs JAG**, **Glavy JS**, **Hurt E and Beck M** (2016) Molecular architecture of the inner ring scaffold of the human nuclear pore complex. *Science* **352**(6283), 363–365.

Kuhlbrandt W (2014) Biochemistry. The resolution revolution. *Science* **343** (6178), 1443–1444.

Langmore JP and Smith MF (1992) Quantitative energy-filtered electron microscopy of biological molecules in ice. *Ultramicroscopy* **46**(1–4), 349–373.

Lasker K, **Forster F**, **Bohn S**, **Walzthoeni T**, **Villa E**, **Unverdorben P**, **Beck F**, **Aebersold R**, **Sali A and Baumeister W** (2012) Molecular architecture of the 26S proteasome holocomplex determined by an integrative approach. *Proc Natl Acad Sci U S A* **109**(5), 1380–1387.

Le Gros MA, **McDermott G**, **Uchida M**, **Knoechel CG and Larabell CA** (2009) High-aperture cryogenic light microscopy. *J Microsc* **235**(1), 1–8.

Lepault J, **Booy FP and Dubochet J** (1983) Electron microscopy of frozen biological suspensions. *J Microsc* **129**(Pt 1), 89–102.

Leunissen JL and Yi H (2009) Self-pressurized rapid freezing (SPRF): A novel cryofixation method for specimen preparation in electron microscopy. *J Microsc* **235**(1), 25–35.

Li S, **Ji G**, **Shi Y**, **Klausen LH**, **Niu T**, **Wang S**, **Huang X**, **Ding W**, **Zhang X**, **Dong M**, **Xu W and Sun F** (2018) High-vacuum optical platform for cryo-CLEM (HOPE): A new solution for non-integrated multiscale correlative light and electron microscopy. *J Struct Biol* **201**(1), 63–75.

Li X, **Mooney P**, **Zheng S**, **Booth CR**, **Braunfeld MB**, **Gubbens S**, **Agard DA and Cheng Y** (2013*a*) Electron counting and beam-induced motion correction enable near-atomic-resolution single-particle cryo-EM. *Nat Methods* **10**(6), 584–590.

Li X, **Zheng SQ**, **Egami K**, **Agard DA and Cheng Y** (2013*b*) Influence of electron dose rate on electron counting images recorded with the K2 camera. *J Struct Biol* **184**(2), 251–260.

Liang YL, **Khoshouei M**, **Radjainia M**, **Zhang Y**, **Glukhova A**, **Tarrasch J**, **Thal DM**, **Furness SGB**, **Christopoulos G**, **Coudrat T**, **Danev R**, **Baumeister W**, **Miller LJ**, **Christopoulos A**, **Kobilka BK**, **Wootten D**, **Skiniotis G and Sexton PM** (2017) Phase-plate cryo-EM structure of a class B GPCR-G-protein complex. *Nature* **546**(7656), 118–123.

Liao M, **Cao E**, **Julius D and Cheng Y** (2013) Structure of the TRPV1 ion channel determined by electron cryo-microscopy. *Nature* **504**(7478), 107–112.

Linke D (2009) Detergents: An overview. *Methods Enzymol* **463**, 603–617.

Liu B, **Xue Y**, **Zhao W**, **Chen Y**, **Fan C**, **Gu L**, **Zhang Y**, **Zhang X**, **Sun L**, **Huang X**, **Ding W**, **Sun F**, **Ji W and Xu T** (2015) Three-dimensional super-resolution protein localization correlated with vitrified cellular context. *Sci Rep* **5**, 13017.

Liu Y, **Gonen S**, **Gonen T and Yeates TO** (2018) Near-atomic cryo-EM imaging of a small protein displayed on a designed scaffolding system. *Proc Natl Acad Sci USA*, 201718825.

Llaguno MC, **Xu H**, **Shi L**, **Huang N**, **Zhang H**, **Liu Q and Jiang QX** (2014) Chemically functionalized carbon films for single molecule imaging. *J Struct Biol* **185**(3), 405–417.

Lu P, **Bai XC**, **Ma D**, **Xie T**, **Yan C**, **Sun L**, **Yang G**, **Zhao Y**, **Zhou R**, **Scheres SH and Shi Y** (2014*a*) Three-dimensional structure of human gamma-secretase. *Nature* **512**(7513), 166–170.

Lu Z, **Barnard D**, **Shaikh TR**, **Meng X**, **Mannella CA**, **Yassin A**, **Agrawal R**, **Wagenknecht T and Lu TM** (2014*b*) Gas-assisted annular microsprayer for sample preparation for time-resolved cryo-electron microscopy. *J Micromech Microeng* **24**(11), 115001.

Lu Z, **Shaikh TR**, **Barnard D**, **Meng X**, **Mohamed H**, **Yassin A**, **Mannella CA**, **Agrawal RK**, **Lu TM and Wagenknecht T** (2009) Monolithic microfluidic mixing-spraying devices for time-resolved cryo-electron microscopy. *J Struct Biol* **168**(3), 388–395.

Lyons JA, **Bøggild A**, **Nissen P and Frauenfeld J** (2017) Chapter Three – Saposin-lipoprotein scaffolds for structure determination of membrane transporters. In: *Methods Enzymol*, Ziegler C (Ed.), pp. 85–99. Oxford, UK: Academic Press.

Lyumkis D, **Julien JP**, **de Val N**, **Cupo A**, **Potter CS**, **Klasse PJ**, **Burton DR**, **Sanders RW**, **Moore JP**, **Carragher B**, **Wilson IA and Ward AB** (2013) Cryo-EM structure of a fully glycosylated soluble cleaved HIV-1 envelope trimer. *Science* **342**(6165), 1484–1490.

Mahamid J, **Pfeffer S**, **Schaffer M**, **Villa E**, **Danev R**, **Cuellar LK**, **Forster F**, **Hyman AA**, **Plitzko JM and Baumeister W** (2016) Visualizing the molecular sociology at the HeLa cell nuclear periphery. *Science* **351**(6276), 969–972.

Mahamid J, **Schampers R**, **Persoon H**, **Hyman AA**, **Baumeister W and Plitzko JM** (2015) A focused ion beam milling and lift-out approach for site-specific preparation of frozen-hydrated lamellas from multicellular organisms. *J Struct Biol* **192**(2), 262–269.

Majorovits E, **Barton B**, **Schultheiss K**, **Perez-Willard F**, **Gerthsen D and Schroder RR** (2007) Optimizing phase contrast in transmission electron microscopy with an electrostatic (Boersch) phase plate. *Ultramicroscopy* **107**(2–3), 213–226.

Marko M, **Hsieh C**, **Schalek R**, **Frank J and Mannella C** (2007) Focused-ion-beam thinning of frozen-hydrated biological specimens for cryo-electron microscopy. *Nat Methods* **4**(3), 215–217.

Martin TG, **Bharat TA**, **Joerger AC**, **Bai XC**, **Praetorius F**, **Fersht AR**, **Dietz H and Scheres SH** (2016) Design of a molecular support for cryo-EM structure determination. *Proc Natl Acad Sci U S A* **113**(47), E7456–e7463.

Matthies D, **Dalmas O**, **Borgnia MJ**, **Dominik PK**, **Merk A**, **Rao P**, **Reddy BG**, **Islam S**, **Bartesaghi A**, **Perozo E and Subramaniam S** (2016) Cryo-EM structures of the magnesium channel CorA reveal symmetry break upon gating. *Cell* **164**(4), 747–756.

McDowall AW, **Chang JJ**, **Freeman R**, **Lepault J**, **Walter CA and Dubochet J** (1983) Electron microscopy of frozen hydrated sections of vitreous ice and vitrified biological samples. *J Microsc* **131**(Pt 1), 1–9.

McMullan G, **Chen S**, **Henderson R and Faruqi AR** (2009*a*) Detective quantum efficiency of electron area detectors in electron microscopy. *Ultramicroscopy* **109**(9), 1126–1143.

McMullan G, **Clark AT**, **Turchetta R and Faruqi AR** (2009*b*) Enhanced imaging in low dose electron microscopy using electron counting. *Ultramicroscopy* **109**(12), 1411–1416.

McMullan G, **Faruqi AR**, **Clare D and Henderson R** (2014) Comparison of optimal performance at 300keV of three direct electron detectors for use in low dose electron microscopy. *Ultramicroscopy* **147**, 156–163.

McMullan G, **Faruqi AR and Henderson R** (2016) Direct electron detectors. *Methods Enzymol* **579**, 1–17.

McMullan G, **Faruqi AR**, **Henderson R**, **Guerrini N**, **Turchetta R**, **Jacobs A and van Hoften G** (2009c) Experimental observation of the improvement in MTF from backthinning a CMOS direct electron detector. *Ultramicroscopy* **109**(9–3), 1144–1147.

https://doi.org/10.1017/S1431927618012382 Published online by Cambridge University Press

Merk A, Bartesaghi A, Banerjee S, Falconieri V, Rao P, Davis MI, Pragani R, Boxer MB, Earl LA, Milne JLS and Subramaniam S (2016) Breaking cryo-EM resolution barriers to facilitate drug discovery. *Cell* **165**(7), 1698–1707.

Meyerson JR, Rao P, Kumar J, Chittori S, Banerjee S, Pierson J, Mayer ML and Subramaniam S (2014) Self-assembled monolayers improve protein distribution on holey carbon cryo-EM supports. *Sci Rep* **4**, 7084.

Milazzo AC, Cheng A, Moeller A, Lyumkis D, Jacovetty E, Polukas J, Ellisman MH, Xuong NH, Carragher B and Potter CS (2011) Initial evaluation of a direct detection device detector for single particle cryo-electron microscopy. *J Struct Biol* **176**(3), 404–408.

Moerner WE and Orrit M (1999) Illuminating single molecules in condensed matter. *Science* **283**(5408), 1670–1676.

Murata K, Liu X, Danev R, Jakana J, Schmid MF, King J, Nagayama K and Chiu W (2010) Zernike phase contrast cryo-electron microscopy and tomography for structure determination at nanometer and subnanometer resolutions. *Structure* **18**(8), 903–912.

Murata K and Wolf M (2018) Cryo-electron microscopy for structural analysis of dynamic biological macromolecules. *Biochim Biophys Acta, Gen Subj* **1862**(2), 324–334.

Nagayama K (2005) Phase contrast enhancement with phase plates in electron microscopy. In: *Advances in Imaging and Electron Physics*, Hawkes PW (Ed.), pp. 69–146. Oxford, UK: Elsevier.

Nagayama K (2011) Another 60 years in electron microscopy: Development of phase-plate electron microscopy and biological applications. *J Electron Microsc* **60**(Suppl 1), S43–S62.

Nagayama K and Danev R (2008) Phase contrast electron microscopy: Development of thin-film phase plates and biological applications. *Philos Trans R Soc B Biol Sci* **363**(1500), 2153–2162.

Noble AJ, Dandey VP, Wei H, Brasch J, Chase J, Acharya P, Tan YZ, Zhang Z, Kim LY, Scapin G, Rapp M, Eng ET, Rice WJ, Cheng A, Negro CJ, Shapiro L, Kwong PD, Jeruzalmi D, des Georges A, Potter CS and Carragher B (2018) Routine single particle CryoEM sample and grid characterization by tomography. *eLife* 7, e34257.

Nogales E (2015) The development of cryo-EM into a mainstream structural biology technique. *Nat Methods* **13**, 24.

Oikonomou CM and Jensen GJ (2017) Cellular electron cryotomography: Toward structural biology in situ. *Ann Rev Biochem* **86**(1), 873–896.

Parent KN, Tang J, Cardone G, Gilcrease EB, Janssen ME, Olson NH, Casjens SR and Baker TS (2014) Three-dimensional reconstructions of the bacteriophage CUS-3 virion reveal a conserved coat protein I-domain but a distinct tailspike receptor-binding domain. *Virology* **464–465**, 55–66.

Parmar M, Rawson S, Scarff CA, Goldman A, Dafforn TR, Muench SP and Postis VLG (2018) Using a SMALP platform to determine a sub-nm single particle cryo-EM membrane protein structure. *Biochim Biophys Acta* **1860**(2), 378–383.

Razinkov I, Dandey V, Wei H, Zhang Z, Melnekoff D, Rice WJ, Wigge C, Potter CS and Carragher B (2016) A new method for vitrifying samples for cryoEM. *J Struct Biol* **195**(2), 190–198.

Rhinow D and Kuhlbrandt W (2008) Electron cryo-microscopy of biological specimens on conductive titanium-silicon metal glass films. *Ultramicroscopy* **108**(7), 698–705.

Rigort A, Bauerlein FJ, Leis A, Gruska M, Hoffmann C, Laugks T, Bohm U, Eibauer M, Gnaegi H, Baumeister W and Plitzko JM (2010) Micromachining tools and correlative approaches for cellular cryo-electron tomography. *J Struct Biol* **172**(2), 169–179.

Rigort A, Villa E, Bäuerlein FJB, Engel BD and Plitzko JM (2012) Chapter 14 – Integrative approaches for cellular cryo-electron tomography: Correlative imaging and focused ion beam micromachining. In: *Methods in Cell Biology*, Müller-Reichert T and Verkade P (Eds), pp. 259–281. Oxford, UK: Academic Press.

Rohou A and Grigorieff N (2015) CTFFIND4: Fast and accurate defocus estimation from electron micrographs. *J Struct Biol* **192**(2), 216–221.

Russo CJ and Passmore LA (2014*a*) Controlling protein adsorption on graphene for cryo-EM using low-energy hydrogen plasmas. *Nat Methods* **11**(6), 649–652.

Russo CJ and Passmore LA (2014*b*) Electron microscopy: Ultrastable gold substrates for electron cryomicroscopy. *Science* **346**(6215), 1377–1380.

Russo CJ and Passmore LA (2016*a*) Progress towards an optimal specimen support for electron cryomicroscopy. *Curr Opin Struct Biol* **37**, 81–89.

Russo CJ and Passmore LA (2016*b*) Ultrastable gold substrates: Properties of a support for high-resolution electron cryomicroscopy of biological specimens. *J Struct Biol* **193**(1), 33–44.

Sander B, Golas MM and Stark H (2005) Advantages of CCD detectors for de novo three-dimensional structure determination in single-particle electron microscopy. *J Struct Biol* **151**(1), 92–105.

Sartori A, Gatz R, Beck F, Rigort A, Baumeister W and Plitzko JM (2007) Correlative microscopy: Bridging the gap between fluorescence light microscopy and cryo-electron tomography. *J Struct Biol* **160**(2), 135–145.

Schellenberger P, Kaufmann R, Siebert CA, Hagen C, Wodrich H and Grunewald K (2014) High-precision correlative fluorescence and electron cryo microscopy using two independent alignment markers. *Ultramicroscopy* **143**, 41–51.

Schmidt C and Urlaub H (2017) Combining cryo-electron microscopy (cryo-EM) and cross-linking mass spectrometry (CX-MS) for structural elucidation of large protein assemblies. *Curr Opin Struct Biol* **46**, 157–168.

Schorb M and Briggs JA (2014) Correlated cryo-fluorescence and cryo-electron microscopy with high spatial precision and improved sensitivity. *Ultramicroscopy* **143**, 24–32.

Schorb M, Gaechter L, Avinoam O, Sieckmann F, Clarke M, Bebeacua C, Bykov YS, Sonnen AFP, Lihl R and Briggs JAG (2017) New hardware and workflows for semi-automated correlative cryo-fluorescence and cryo-electron microscopy/tomography. *J Struct Biol* **197**(2), 83–93.

Schroder RR (1992) Zero-loss energy-filtered imaging of frozen-hydrated proteins: Model calculations and implications for future developments. *J Microsc* **166**(Pt 3), 389–400.

Schroder RR (2015) Advances in electron microscopy: A qualitative view of instrumentation development for macromolecular imaging and tomography. *Arch Biochem Biophys* **581**, 25–38.

Schultheiss K, Zach J, Gamm B, Dries M, Frindt N, Schröder RR and Gerthsen D (2010) New electrostatic phase plate for phase-contrast transmission electron microscopy and its application for wave-function reconstruction. *Microsc Microanal* **16**(6), 785–794.

Schwartz CL, Sarbash VI, Ataullakhanov FI, McIntosh JR and Nicastro D (2007) Cryo-fluorescence microscopy facilitates correlations between light and cryo-electron microscopy and reduces the rate of photobleaching. *J Microsc* **227**(2), 98–109.

Shaikh TR, Yassin AS, Lu Z, Barnard D, Meng X, Lu TM, Wagenknecht T and Agrawal RK (2014) Initial bridges between two ribosomal subunits are formed within 9.4 milliseconds, as studied by time-resolved cryo-EM. *Proc Natl Acad Sci U S A* **111**(27), 9822–9827.

Sharp TH, Koster AJ and Gros P (2016) Heterogeneous MAC initiator and pore structures in a lipid bilayer by phase-plate cryo-electron tomography. *Cell Rep* **15**(1), 1–8.

Shen PS, Yang X, DeCaen PG, Liu X, Bulkley D, Clapham DE and Cao E (2016) The structure of the polycystic kidney disease channel PKD2 in lipid nanodiscs. *Cell* **167**(3), 763–773.e711.

Stagg SM, Lander GC, Pulokas J, Fellmann D, Cheng A, Quispe JD, Mallick SP, Avila RM, Carragher B and Potter CS (2006) Automated cryoEM data acquisition and analysis of 284742 particles of GroEL. *J Struct Biol* **155**(3), 470–481.

Stark H (2010) GraFix: Stabilization of fragile macromolecular complexes for single particle cryo-EM. *Methods Enzymol* **481**, 109–126.

Strauss JD, Hammonds JE, Yi H, Ding L, Spearman P and Wright ER (2016) Three-dimensional structural characterization of HIV-1 tethered to human cells. *J Virol* **90**(3), 1507–1521.

Studer D, Humbel BM and Chiquet M (2008) Electron microscopy of high pressure frozen samples: Bridging the gap between cellular ultrastructure and atomic resolution. *Histochem Cell Biol* **130**(5), 877–889.

Subramaniam S, Kuhlbrandt W and Henderson R (2016) CryoEM at IUCrJ: A new era. *IUCrJ* **3**(Pt 1), 3–7.

Sun C, Benlekbir S, Venkatakrishnan P, Wang Y, Hong S, Hosler J, Tajkhorshid E, Rubinstein JL and Gennis RB (2018) Structure of the alternative complex III in a supercomplex with cytochrome oxidase. *Nature* **557**(7703), 123–126.

https://doi.org/10.1017/S1431927618012382 Published online by Cambridge University Press

Tan YZ, Baldwin PR, Davis JH, Williamson JR, Potter CS, Carragher B and Lyumkis D (2017) Addressing preferred specimen orientation in single-particle cryo-EM through tilting. *Nat Methods* **14**(8), 793–796.

Tanner JRD, Demmart AC, Dukes MJ, Melanson LA, McDonald SM and Kelly DF (2013) Cryo-SiN – An alternative substrate to visualize active viral assemblies. *J Analyt Molecul Tech* **1**(1), 6.

Taylor KA and Glaeser RM (1974) Electron diffraction of frozen, hydrated protein crystals. *Science* **186**(4168), 1036–1037.

Thompson RF, Walker M, Siebert CA, Muench SP and Ranson NA (2016) An introduction to sample preparation and imaging by cryo-electron microscopy for structural biology. *Methods* **100**, 3–15.

Unwin N (1995) Acetylcholine receptor channel imaged in the open state. *Nature* **373**(6509), 37–43.

Unwin N and Fujiyoshi Y (2012) Gating movement of acetylcholine receptor caught by plunge-freezing. *J Mol Biol* **422**(5), 617–634.

van Driel LF, Valentijn JA, Valentijn KM, Koning RI and Koster AJ (2009) Tools for correlative cryo-fluorescence microscopy and cryo-electron tomography applied to whole mitochondria in human endothelial cells. *Eur J Cell Biol* **88**(11), 669–684.

von der Ecken J, Muller M, Lehman W, Manstein DJ, Penczek PA and Raunser S (2015) Structure of the F-actin-tropomyosin complex. *Nature* **519**(7541), 114–117.

von Loeffelholz O, Papai G, Danev R, Myasnikov AG, Natchiar SK, Hazemann I, Menetret JF and Klaholz BP (2018) Volta phase plate data collection facilitates image processing and cryo-EM structure determination. *J Struct Biol* **202**(3), 191–199.

Voorhees RM, Fernandez IS, Scheres SH and Hegde RS (2014) Structure of the mammalian ribosome-Sec61 complex to 3.4 Å resolution. *Cell* **157**(7), 1632–1643.

Walker M, Trinick J and White H (1995) Millisecond time resolution electron cryo-microscopy of the M-ATP transient kinetic state of the acto-myosin ATPase. *Biophys J* **68**(4 Suppl), 87S–91S.

Walker M, Zhang X-Z, Jiang W, Trinick J and White HD (1999) Observation of transient disorder during myosin subfragment-1 binding to actin by stopped-flow fluorescence and millisecond time resolution electron cryomicroscopy: Evidence that the start of the crossbridge power stroke in muscle has variable geometry. *Proc Natl Acad Sci U S A* **96**(2), 465–470.

Walter A, Muzik H, Vieker H, Turchanin A, Beyer A, Golzhauser A, Lacher M, Steltenkamp S, Schmitz S, Holik P, Kuhlbrandt W and Rhinow D (2012) Practical aspects of Boersch phase contrast electron microscopy of biological specimens. *Ultramicroscopy* **116**, 62–72.

Wan RX, Yan CY, Bai R, Wang L, Huang M, Wong CCL and Shi YG (2016) The 3.8 angstrom structure of the U4/U6.U5 tri-snRNP: Insights into spliceosome assembly and catalysis. *Science* **351**(6272), 466–475.

Wan W and Briggs JAG (2016) Chapter Thirteen – Cryo-electron tomography and subtomogram averaging. In: *Methods in Enzymology*, Crowther RA (Ed.), pp. 329–367. Oxford, UK: Academic Press.

Wang L, Ounjai P and Sigworth FJ (2008) Streptavidin crystals as nanostructured supports and image-calibration references for cryo-EM data collection. *J Struct Biol* **164**(2), 190–198.

Wei H, Dandey VP, Zhang Z, Raczkowski A, Rice WJ, Carragher B and Potter CS (2018) Optimizing "self-wicking" nanowire grids. *J Struct Biol* **202**(2), 170–174.

Wilkes M, Madej MG, Kreuter L, Rhinow D, Heinz V, De Sanctis S, Ruppel S, Richter RM, Joos F, Grieben M, Pike ACW, Huiskonen JT, Carpenter EP, Kühlbrandt W, Witzgall R and Ziegler C (2017) Molecular insights into lipid-assisted Ca2 + regulation of the TRP channel Polycystin-2. *Nat Struct Mol Biol* **24**, 123.

Wolf SG, Mutsafi Y, Horowitz B, Elbaum M and Fass D (2016) Cryo-Stem tomography provides morphological and chemical characterization of precipitated calcium-phosphate clusters sequestered in mitochondria of intact vitrified fibroblasts. *Biophys J* **110**(3), 23a.

Yoshioka C, Carragher B and Potter CS (2010) Cryomesh: A new substrate for cryo-electron microscopy. *Microsc Microanal* **16**(1), 43–53.

Yu G, Li K, Huang P, Jiang X and Jiang W (2016*a*) Antibody-based affinity cryoelectron microscopy at 2.6-Å resolution. *Structure* **24**(11), 1984–1990.

Yu G, Li K and Jiang W (2016*b*) Antibody-based affinity cryo-EM grid. *Methods* **100**, 16–24.

Yu G, Vago F, Zhang D, Snyder JE, Yan R, Zhang C, Benjamin C, Jiang X, Kuhn RJ, Serwer P, Thompson DH and Jiang W (2014) Single-step antibody-based affinity cryo-electron microscopy for imaging and structural analysis of macromolecular assemblies. *J Struct Biol* **187**(1), 1–9.

Zhang J, Ma B, DiMaio F, Douglas NR, Joachimiak LA, Baker D, Frydman J, Levitt M and Chiu W (2011) Cryo-EM structure of a Group II chaperonin in the prehydrolysis ATP-bound state leading to lid closure. *Structure* **19**(5), 633–639.

Zhang P (2013) Correlative Cryo-electron tomography and optical microscopy of cells. *Curr Opin Struct Biol* **23**(5), 763–770.

https://doi.org/10.1017/S1431927618012382 Published online by Cambridge University Press